Available online at www.sciencedirect.com
ScienceDirect
Geochimica et Cosmochimica Acta xxx (2007) xxx–xxx
Geochimica et Cosmochimica Acta
www.elsevier.com/locate/gca

Valence of titanium and vanadium in pyroxene in refractory inclusion interiors and rims

S.B. Simon [a,*], S.R. Sutton [a,b], L. Grossman [a,c]

[a] Department of the Geophysical Sciences, 5734 S. Ellis Ave., The University of Chicago, Chicago, IL 60637, USA
[b] Center for Advanced Radiation Sources, 5640 S. Ellis Ave., The University of Chicago, Chicago, IL 60637, USA
[c] The Enrico Fermi Institute, 5640 S. Ellis Ave., The University of Chicago, Chicago, IL 60637, USA

Received 18 December 2006; accepted in revised form 30 March 2007

Abstract

The clinopyroxene in coarse-grained refractory inclusions contains significant amounts of Ti and V, two elements that are multivalent over the range of temperatures and oxygen fugacities under which the inclusions formed. The Ti^{3+}/Ti^{4+} ratios and the valence of V of these pyroxenes are valuable recorders of nebular conditions. The former can be calculated stoichiometrically from electron probe analyses, but only for relatively Ti-rich grains (i.e., $>\sim$4 wt% TiO_2^{tot}). For Ti-poor pyroxene, and for measurement of V valence, another technique is needed. We have, for the first time, applied K-edge X-ray absorption near edge structure (XANES) spectroscopy to the measurement of Ti and V valence in meteoritic clinopyroxene in refractory inclusions. Use of MicroXANES, a microbeam technique with high (μm-scale) spatial resolution, allowed measurement of Ti and V valence along traverses across (a) Ti-, V-rich "spikes" in pyroxene in Type B1 inclusions; (b) typical grains in a Type B2 inclusion; and (c) the pyroxene layer of the Wark–Lovering rim sequence on the outsides of two inclusions. Measurements of $Ti^{3+}/(Ti^{3+}+Ti^{4+})$, or Ti^{3+}/Ti^{tot}, by XANES agree with values calculated from electron probe analyses to within $\sim$0.1, or $\sim 2\sigma$. The results show that Ti^{3+}/Ti^{tot} increases sharply at the spikes, from 0.46 ± 0.03 to 0.86 ± 0.06, but the V valence, or $V^{2+}/(V^{2+}+V^{3+})$, does not change, with $V^{2+} \approx V^{3+}$. We found that pyroxene in both Types B1 and B2 inclusions has Ti^{3+}/Ti^{tot} and V^{2+}/V^{tot} ratios between 0.4 and 0.7, except for the spikes. These values indicate, to first order, formation at similar, highly reducing oxygen fugacities that are consistent with a solar gas. The pyroxene in the rim on an Allende fluffy Type A coarse-grained refractory inclusion, TS24, has an average Ti^{3+}/Ti^{tot} of 0.51 ± 0.08 and an average V^{2+}/V^{tot} of 0.61 ± 0.06, determined by XANES. These values are within the range of those of pyroxene in the interiors of inclusions, indicating that the rims also formed under highly reducing conditions. Measurements of Ti^{3+}/Ti^{tot} of pyroxene in the rim of a Leoville compact Type A inclusion, 144A, by both XANES and electron probe give a wide range of results. Of our 72 XANES analyses of this rim, 66% have Ti^{3+}/Ti^{tot} of 0.40–0.71, and the remaining analyses range from 0 to 0.38. In data from Simon et al. [Simon J. I., Young E. D., Russell S. S., Tonui E. K., Dyl K. A., and Manning C. E. (2005) A short timescale for changing oxygen fugacity in the solar nebula revealed by high-resolution ^{26}Al–^{26}Mg dating of CAI rims. *Earth Planet. Sci. Lett.* **238**, 272–283.] for this sample, 7 electron probe analyses yield calculated Ti^{3+}/Ti^{tot} values that are positive and 15 do not. In the probe analyses that have no calculated Ti^{3+}, Ca contents are anticorrelated and Al contents directly correlated with the total cations per 6 oxygens, and the data fall along trends calculated for addition of 1–7% spinel to pyroxene. It appears likely that electron probe analyses of pure pyroxene spots have Ti^{3+}/Ti^{tot} values that are typical of refractory inclusions, in agreement with the majority of the XANES results. The average of the XANES data for 144A, 0.41 ± 0.14, is within error of that for TS24. The rim of 144A probably formed under reducing conditions like those expected for a solar gas, and was later heterogeneously altered, resulting in an uneven distribution of secondary, FeO-, Ti-bearing alteration products in the rim, and accounting for the measurements with low Ti^{3+}/Ti^{tot} values.

* Corresponding author. Fax: +1 773 702 9505.
E-mail address: sbs8@uchicago.edu (S.B. Simon).

0016-7037/$ - see front matter © 2007 Elsevier Ltd. All rights reserved.
doi:10.1016/j.gca.2007.03.027

1. INTRODUCTION

The two major types of coarse-grained, calcium-, aluminum-rich refractory inclusions (CAI) found in carbonaceous chondrites were termed Types A and B by Grossman (1975). Type A inclusions are very melilite-rich (>75 vol %), with minor amounts of Mg-, Al- spinel, perovskite, and Ti-, Al-rich clinopyroxene termed "fassaite" (Dowty and Clark, 1973). On the basis of texture, Type As are subdivided into "compact" Type As, or CTAs, which are thought to have been molten, and "fluffy" Type As, which were probably never molten (MacPherson and Grossman, 1979; Grossman, 1980). Type Bs contain 25–60 vol % fassaite plus 5–50% melilite, 15–30% Mg-, Al-spinel, and 5–25% anorthite. Wark and Lovering (1977) further subdivided Type Bs into B1s, which have nearly monomineralic melilite mantles enclosing pyroxene-rich cores, and B2s, which have relatively homogeneous distributions of phases. Type B inclusions are believed to have crystallized from liquids formed by partial melting of preexisting solids (Stolper and Paque, 1986), which were probably nebular condensates (Grossman, 1972). Pyroxene is an excellent recorder of changes in liquid composition during crystallization of melts, including those from which these inclusions solidified. Simon et al. (1991) showed that core-to-rim zoning trends in fassaite in Type B inclusions are consistent with fractional crystallization and reflect the buildup of incompatible trace elements that occurred in the residual liquids during crystallization.

The environment in which refractory inclusions formed was very reducing, and fassaite is of interest as an indicator of oxygen fugacity (f_{O_2}) because it is rich in Ti, about half of which in the pyroxene in inclusion interiors is trivalent, rather than being all Ti^{4+} as is found in terrestrial and lunar samples. Evidence for the presence of Ti^{3+} in meteoritic fassaite includes pleochroism of the crystals, which have negligible amounts of other multivalent elements; measurements of optical spectra (Dowty and Clark, 1973); and systematically low cation totals derived from electron probe analyses when all Ti is assumed to be Ti^{4+}, commonly referred to as $TiO_2{}^{tot}$. If the presence of trivalent Ti is ignored when analyses are normalized to a fixed number of oxygen anions, too much oxygen is assigned to the measured Ti and a low cation:oxygen ratio is obtained.

In an electron probe study of zoning trends in coarse fassaite in Type B inclusions, Simon et al. (1991) found that Ti_2O_3 contents of the grains tended to decrease from crystal cores to the rims. Simon et al. (1991) also showed that the trend of decreasing Ti_2O_3 contents could be accounted for by the high (~3) crystal/liquid distribution coefficient (D) for Ti^{3+} relative to that of Ti^{4+} (~1); as crystallization proceeded, Ti^{3+} became depleted in the liquid, apparently without replenishment by reduction of Ti^{4+}.

Detailed study has shown, however, that superimposed upon the otherwise smooth decline in Ti_2O_3 in some large (~2 mm) fassaite grains in several Allende Type B1 inclusions are "spikes", or sharp increases, in total Ti, $Ti^{3+}/(Ti^{3+} + Ti^{4+})$ or Ti^{3+}/Ti^{tot}, and in the concentration of V (Simon and Grossman, 1991, 2006; Simon et al., 1992). Because the two elements that exhibit spikes can be multivalent at f_{O_2}s calculated for a system of solar composition, it was suggested by Simon et al. (1992) that the spikes reflect sudden decreases in the f_{O_2}s of the inclusions, caused by re-establishment of chemical communication between the nebular gas and late liquids, perhaps by means of cracks in the solid melilite mantles of these objects. Simon et al. (1992) did not know what oxidation states of V were involved, or which would be favored by fassaite. Simon and Grossman (2006) showed that, unlike fassaites in Type B1 inclusions, those in B2s are not zoned with respect to Ti^{3+}/Ti^{tot}, and Ti-, V-enrichment spikes are not seen in traverses across grains. This suggests that the residual liquids in B2s maintained equilibrium with the surrounding, reducing nebular gas, while those in B1s did not. The average Ti^{3+}/Ti^{tot} for electron probe analyses of Type B1 fassaite is within 1σ of that for fassaite in Type B2 inclusions (Simon and Grossman, 2006). A question to be answered is whether the V^{2+}/V^{tot} ratios are similar as well.

Because V is a stoichiometrically insignificant component in fassaite and it occurs in a phase with both Ti^{3+} and Ti^{4+}, the valence of V cannot be calculated from electron probe analyses. Thus, until now it has not been possible to determine what, if any, change occurs in the $V^{2+}/(V^{2+} + V^{3+})$, henceforth V^{2+}/V^{tot}, of fassaite at the spikes. An alternative approach to determine the valence of Ti and V is to use X-ray Absorption Near Edge Structure (XANES) spectroscopy. Applicability of this technique to lunar, martian, and terrestrial samples, with V^{3+} and V^{4+}, has been documented (Sutton et al., 2005). Herein we apply this technique, for the first time, to the determination of Ti and V valence states in natural samples formed within the range of V^{2+} and Ti^{3+} stability. In addition to the direct measurement of Ti and V valence variations across spikes in fassaite in Type B1 inclusions, we also report measurements of V valence in traverses across fassaite crystals in a Type B2 inclusion, for comparison with the B1 measurements.

Ti-bearing pyroxene also occurs as part of a sequence of monomineralic layers on the exteriors of inclusions, as originally described by Wark and Lovering (1977). We used XANES to directly measure, for the first time, Ti and V valence in pyroxene in the Wark–Lovering rims on two Type A inclusions, a fluffy one from Allende (TS24) and a compact one from Leoville (144A). Recent work by Dyl et al. (2005) and J. Simon et al. (2005) on the latter sample reported undetectable levels of Ti^{3+} in Ti-bearing pyroxene in its rim, and concluded that the oxygen fugacity of the solar nebula increased dramatically between the time of formation of pyroxene in the interiors of inclusions and that of the rim pyroxene. The Ti^{3+} contents reported in that paper were derived from electron probe analyses. Preliminary results of the present work were reported by Sutton et al. (2002a) and by S. Simon et al. (2005, 2006).

2. ANALYTICAL AND DATA REDUCTION METHODS

2.1. Electron microbeam

A JEOL JSM-5800LV scanning electron microscope (SEM) equipped with an Oxford/Link ISIS-300 energy-dis-

Please cite this article in press as: Simon S. B. et al, Valence of titanium and vanadium in pyroxene ..., *Geochim. Cosmochim. Acta* (2007), doi:10.1016/j.gca.2007.03.027

persive X-ray analysis system was used to obtain backscattered electron images of grains selected for analysis. Quantitative wavelength-dispersive analyses were obtained with a Cameca SX-50 electron microprobe operated at 15 kV with counting times of 10–30 s for peak and for background measurements for each analysis. Pure oxide, synthetic glass, and natural mineral standards were used. Electron probe (EMP) data were reduced via the modified ZAF correction procedure PAP (Pouchou and Pichoir, 1984).

To calculate the Ti^{3+}/Ti^{tot} ratio of a pyroxene from an electron probe analysis, it is assumed that the pyroxene is stoichiometric and has exactly four cations per 6 oxygens. For highest accuracy, it is also assumed that there are exactly two tetrahedral cations and one calcium cation per 6 oxygens (Beckett, 1986). The lower the Ti content of the pyroxene, however, the smaller is the cation deficit caused by assuming all Ti is Ti^{4+}. For TiO_2^{tot} of about 4 wt% and less, the cation deficit approaches the analytical uncertainty and a Ti^{3+}/Ti^{tot} ratio cannot be reliably calculated. This effect limits the use of this technique to fairly Ti-rich pyroxenes. Uncertainties in the Ti^{3+}/Ti^{tot} ratio derived from EMP analyses are based on counting statistics of the analyses propagated through the calculation of the ratio.

2.2. XANES measurements

X-ray absorption near edge structure (XANES) is that portion of an X-ray absorption spectrum within about 40 eV of the main absorption edge jump. XANES spectra are element-specific, and intensities and energies of the XANES spectral features provide information on the electronic structure of the element of interest, including valence state.

Ti and V K XANES spectra were measured using the undulator-based microprobe at Sector 13 (GeoSoilEnviroCARS) at the Advanced Photon Source, Argonne National Laboratory (Sutton and Rivers, 1999). X-ray microprobe techniques are described in detail elsewhere (e.g., Sutton et al., 2002b; Smith and Rivers, 1995). The undulators at third generation synchrotrons (e.g., the APS) are excellent sources for XANES measurements with high sensitivity and high spatial resolution because of the extremely high brilliance of the X-ray source. A Si (111) liquid-nitrogen cooled, double-crystal, scannable monochromator was used. The instrumental energy resolution (0.8 eV) was comparable to the natural Ti and V K line widths (~1 eV; Krause and Oliver, 1979) so that the overall energy resolution of the Ti and V K XANES spectra was about 1.5 eV.

The microbeam production apparatus consists of Kirkpatrick–Baez (KB; Kirkpatrick and Baez, 1948) microfocusing mirrors (Eng et al., 1995, 1998; Yang et al., 1995). The KB system consists of two mirrors (100 mm length), one in the horizontal plane and one in the vertical plane, which collected 300 μm of X-ray beam in each direction and produced a focal spot of ~3 μm in each direction. The mirrors are highly polished single crystal silicon coated with several hundred Å of Rh dynamically bent to elliptical shapes using mechanical benders. XANES spectra were collected in fluorescence mode where the primary excitation beam is the monochromatic undulator radiation, and the X-ray fluorescence emitted by the sample is collected using solid state detectors, either a 16-element Ge array, energy dispersive X-ray fluorescence detector (Canberra Industries, Inc.) or a Vortex-EX Si drift detector (Radiant Detector Technologies LLC). Both of these detectors used digital signal processing electronics with energy resolutions of 130 (Vortex) to 150 eV (Canberra) for Ti and V K fluorescence peaks.

The samples, in the form of polished thin sections (except for one polished chip), were placed on an *x*-*y*-*z* stepping motor stage (1 μm resolution, positioned at 45° to the incident beam), allowing the analysis point of interest to be placed in the monochromatic X-ray beam, as described in Sutton et al. (2005). During the acquisition of XANES spectra, two devices were scanned in unison, the undulator gap (controlling the energy of the fundamental peak in the undulator radiation spectrum) and the monochromator (controlling the excitation energy of fluorescence). The position stability of the beam on the sample (<1 μm) was verified prior to the measurements by viewing the beam on a phosphor screen as these motions were executed.

The typical XANES spectrum was acquired from 5460 to 5600 eV (V) and 4960 to 5100 eV (Ti) with 0.25 (V) and 0.20 (Ti) eV monochromator steps over the pre-edge and edge region. Total acquisition times per energy step varied from 0.5 s to 1 min depending on Ti or V concentration. Energy calibration was obtained from XANES spectra of Ti and V metal foils (EXAFS Materials, Danville, CA). The first peak in the derivative spectrum was defined to be 5465 (V) and 4966 (Ti) eV. In each XANES spectrum, the pre-edge background was subtracted and the difference normalized to the highest count rate within the spectrum.

For both Ti and V, the pre-edge peaks were used for valence determinations. Analysis of the pre-edge region was conducted after subtracting the edge step contribution via an interactive spline-fitting routine. The pre-edge regions consist of several overlapping peaks due to transitions from 1*s* energy levels to bound 3*d* molecular orbitals (e.g., Waychunas, 1987), and the intensities and energies of features are valence sensitive. Titanium valence determinations were made from the ratios of the intensities of the main pre-edge multiplet components at 4969 and 4971 eV, the intensity of the latter being most sensitive to valence variations (Waychunas, 1987). Intensity ratios were determined by Lorentzian peak fitting of the multiplet ensemble. These valence-sensitive variations in intensity are due primarily to modifications in the distortion of the Ti site. Variations in intensity can also arise from differences in site geometry (e.g., tetrahedral vs. octahedral) but such effects are expected to be minimal in this work, where Ti in clinopyroxene is expected to be in octahedral coordination (e.g., Dowty and Clark, 1973). As will be shown below, the concordance of Ti valence state determinations between EMP and XANES for high- Ti fassaite supports this interpretation.

Ti valence standardization was obtained using spectra for endmember silicate standards: Ti^{3+} (synthetic $NaTi^{3+}Si_2O_6$, isostructural with acmite; Prewitt et al., 1972) and Ti^{4+} (natural acmite, Norway; natural titanite, Australia). These standards have multiplet intensity ratios (high energy/low energy) of 0.6 and 2.7, respectively (Waychunas, 1987). Vanadium valence was determined from the absolute

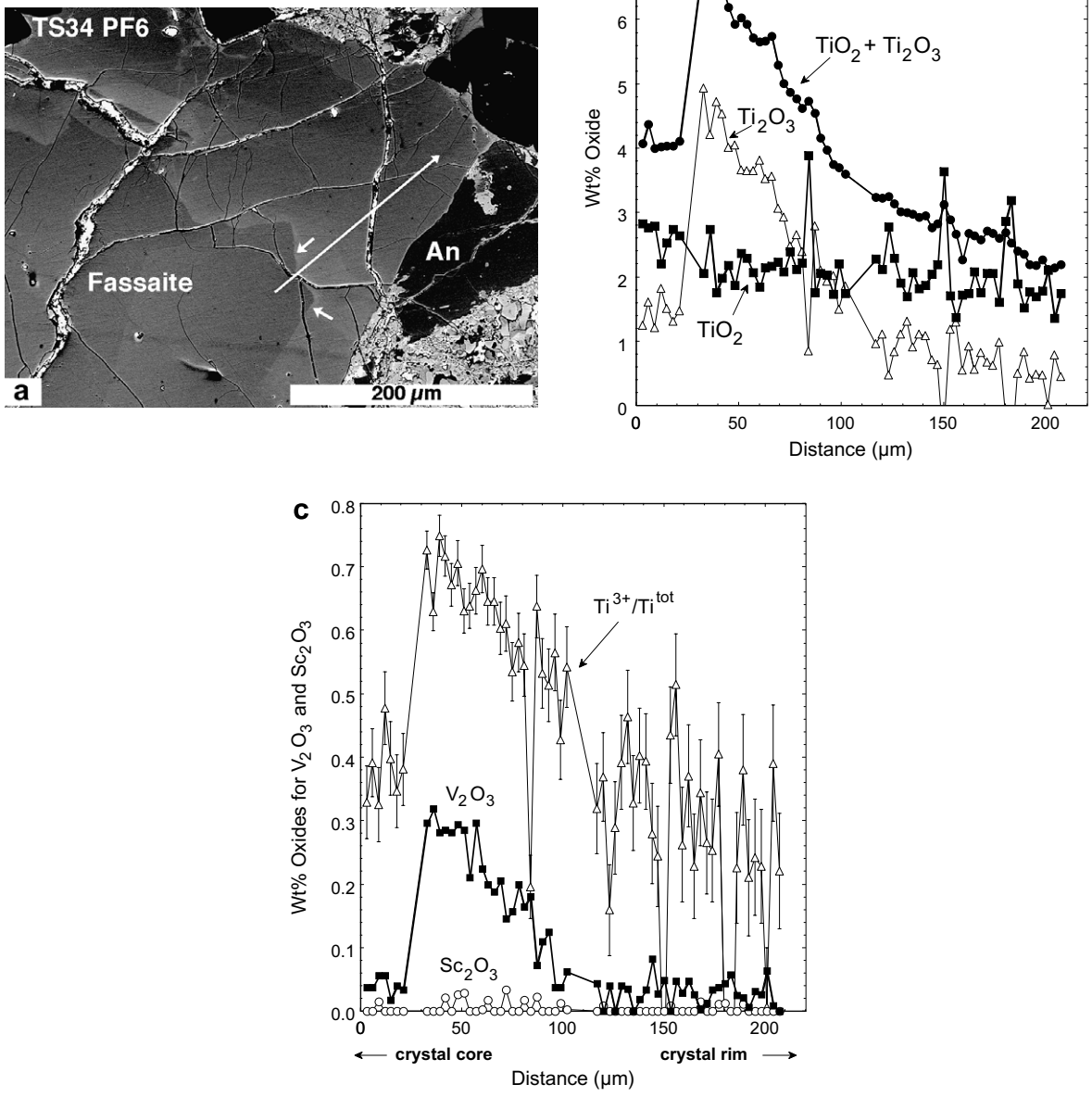

Fig. 1. A Ti-, V-rich spike in a fassaite grain, PF6, in Allende Type B1 inclusion TS34. (a) Backscattered electron image of the outer part of the crystal. Short arrows indicate the sharp contact (location of the "spike") between the lighter, relatively Ti-, V-rich fassaite and the darker, relatively Ti-,V-poor fassaite it encloses. The location of EMP and XANES traverses is indicated by the long arrow. (b) Variation of Ti oxide abundances across the spike for the traverse shown in (a). Note the sharp increases in Ti_2O_3 and in $TiO_2 + Ti_2O_3$. (c) Variation of Ti^{3+}/Ti^{tot}, V_2O_3 and Sc_2O_3 across the spike for the traverse shown in (a). Note the sharp increases in Ti^{3+}/Ti^{tot} and V_2O_3 but not in Sc_2O_3.

intensity of the pre-edge peak ensemble, following the procedure described by Sutton et al. (2005) based on XANES spectra of the basaltic glass standards of Schreiber and Balazs (1982). In the present work, V^{2+} and V^{3+} are the most relevant and these species have pre-edge peak intensities of 0 and 115, respectively (normalized to an absorption edge step of 1000; Sutton et al., 2005). For both elements, the valence of unknowns was determined from linear interpolation of the endmember values.

3. RESULTS

3.1. Fassaite in Type B refractory inclusion interiors

3.1.1. Ti-, V-rich "spikes" in Type B1 inclusions

Electron microprobe and XANES traverses were conducted across spikes in two fassaite crystals, PF6 and ZF2, in Allende inclusion TS34 (B1). Within a given grain, the relatively Ti-, V-rich fassaite is revealed by its high albe-

Table 1
Representative electron microprobe analyses of fassaite from traverse across spike in TS34 PF6

	1	2	3	4	5
MgO	9.98	9.59	9.88	10.86	12.05
Al_2O_3	19.57	16.98	17.95	16.55	15.19
SiO_2	39.92	39.23	40.19	42.03	43.94
CaO	25.26	25.13	25.21	25.38	25.64
$TiO_2{}^{tot}$	4.27	7.47	6.12	4.85	3.07
V_2O_3	0.03	0.30	0.30	0.07	0.03
Cr_2O_3	0.13	0.06	0.04	0.07	0.07
FeO	BDL	BDL	0.04	BDL	BDL
Ti_2O_3	1.46	4.93	3.65	2.79	1.09
TiO_2	2.64	2.06	2.06	1.76	1.86
Sum	99.00	98.29	99.33	99.51	99.88
Cations per 6 oxygen anions					
Si	1.475	1.482	1.489	1.547	1.604
^{IV}Al	0.525	0.518	0.511	0.453	0.396
^{VI}Al	0.327	0.237	0.273	0.265	0.257
Mg	0.549	0.540	0.546	0.596	0.656
Fe	0.000	0.000	0.001	0.000	0.000
V	0.001	0.008	0.008	0.002	0.001
Cr	0.004	0.002	0.001	0.002	0.002
Ti^{3+}	0.045	0.154	0.113	0.086	0.033
Ti^{4+}	0.073	0.058	0.058	0.049	0.051
Ca	1.000	1.000	1.000	1.000	1.000
Ti^{3+}/Ti^{tot}	0.381	0.727	0.663	0.638	0.393

1, Last pre-spike point. 2, First post-spike point, ~12 μm from anal. 1. 3, Post-spike, 25 μm from anal. 2. 4, Post-spike, 55 μm from anal. 2. 5, Post-spike, 108 μm from anal. 2. Analyses are normalized to four total cations, including exactly one Ca and two tetrahedral cations per 6 oxygen anions according to the method of Beckett (1986). Sums include Ti_2O_3 and TiO_2, not $TiO_2{}^{tot}$. BDL, below detection limit of 0.038 wt% FeO. All analyses have Sc_2O_3 contents below the detection limit of 0.037 wt%.

do in backscattered electron images (e.g., Fig. 1a). The contacts between the Ti-, V-rich and Ti-, V-poor fassaite are sharp and irregular. The location of the EMP and XANES traverses in PF6 is indicated by the long arrow in Fig. 1a, which shows that they start in low-albedo, Ti-poor fassaite to the left (interior) of the lighter, relatively Ti-rich fassaite that defines the spike. The traverse path goes across the spike (short arrows) toward the edge of the crystal, so we interpret the starting point as being in pre-spike fassaite. As illustrated in Fig. 1b, the EMP analyses show that at the spike, fassaite Ti_2O_3 contents sharply increase, TiO_2 decreases slightly, and therefore total Ti oxides, $TiO_2 + Ti_2O_3$, also increase sharply. Sharp increases in Ti^{3+}/Ti^{tot} and in V (reported as V_2O_3) are also seen, although Sc_2O_3, also compatible in fassaite (Simon et al., 1991) but with only one valence state, remains flat (Fig. 1c). Because values of Ti^{3+}/Ti^{tot} derived from electron probe analyses with $TiO_2 + Ti_2O_3$ contents $<\sim$4 wt% are poorly defined, the trend of this ratio becomes erratic, with large uncertainties, for the low-Ti fassaite at distances $\geqslant$100 μm into the traverse (Fig. 1c). Representative analyses from the traverse are given in Table 1.

Results of XANES traverses across the same spike are presented in Tables 2 and 3 and are illustrated in Fig. 2. Relative abundances of Ti and V were determined from K_α count rates and are shown for correlation of the measurements with the EMP data and with the location of the spike. The increases in Ti content and in Ti^{3+}/Ti^{tot} are clearly seen. The XANES data also show that Ti^{3+}/Ti^{tot} values did not return to their pre-spike levels after the formation of the spike (Fig. 2b). The late, post-spike fassaite has Ti^{3+}/Ti^{tot} values slightly lower than that at the spike but much higher than in the pre-spike fassaite.

A direct comparison of the Ti valence measurement results using the two methods for this traverse, for analyses from the high-Ti region ($TiO_2{}^{tot} \geqslant 4\%$), is shown in Fig. 2c. The overall agreement is generally good, but the XANES Ti^{3+}/Ti^{tot} data are systematically higher than the EMP by about 0.1, a value whose magnitude is comparable to the 2σ uncertainty (1σ error bars are shown). In the EMP analyses, Ti^{3+}/Ti^{tot} increases from 0.38 ± 0.06 (1σ) to 0.73 ± 0.03 at the spike, and XANES gives 0.46 ± 0.03 and 0.86 ± 0.06 (1σ) for the two points closest to the spike (Fig. 2c).

Results of measurements of V XANES spectra are shown in Fig. 2d and e. The spike in V abundances is clearly detected (Fig. 2d), but a change in V^{2+}/V^{tot} is not observed (Fig. 2e); the results for the latter range from 0.46 ± 0.04 to 0.53 ± 0.03 (1σ), indicating that $V^{2+} \approx V^{3+}$ throughout the traverse.

Results from a XANES traverse across a spike in another crystal from TS34, ZF2, are summarized in Fig. 3. Ti^{3+}/Ti^{tot} increases from 0.36 ± 0.03 to 0.81 ± 0.05 at the spike. Post-spike values are flat at ~0.75 (Fig. 3b) and, as in PF6, are much higher than the pre-spike values of ~0.4. Also like PF6, the increase in V abundance

Table 2
Titanium K XANES data for line scans across the concentration spikes in two interior fassaite grains from Allende

Relative position (μm)	Ti abundance (counts)	Peak ratio	Valence	Ti^{3+}/Ti^{tot}	σ
Allende TS34 ZF2					
0	172,000	1.94	3.63	0.37	0.04
7	191,000	1.78	3.56	0.44	0.05
15	191,000	1.89	3.61	0.39	0.04
22	202,000	1.91	3.62	0.38	0.02
30	200,000	1.96	3.64	0.36	0.03
37	205,000	1.74	3.54	0.46	0.04
45	269,000	1.37	3.36	0.64	0.04
52	288,000	1.18	3.28	0.72	0.04
60	288,000	0.97	3.19	0.81	0.05
67	271,000	0.98	3.20	0.80	0.04
75	252,000	1.03	3.24	0.76	0.05
82	232,000	0.99	3.26	0.74	0.05
90	231,000	1.13	3.27	0.73	0.01
97	216,000	1.14	3.25	0.75	0.01
105	220,000	1.08	3.23	0.77	0.04
112	212,000	1.11	3.24	0.76	0.06
120	230,000	1.07	3.22	0.78	0.04
Allende TS34 PF6					
0	207,000	1.79	3.57	0.43	0.05
20	200,000	1.86	3.60	0.40	0.03
40	193,000	1.77	3.56	0.44	0.03
60	183,000	1.73	3.54	0.46	0.03
80	269,000	0.90	3.14	0.86	0.06
100	242,000	1.00	3.19	0.81	0.08
120	200,000	1.04	3.21	0.79	0.05
140	162,000	1.15	3.26	0.74	0.07
160	122,000	1.32	3.34	0.66	0.03
180	132,000	1.25	3.31	0.69	0.01
200	127,000	1.28	3.32	0.68	0.03

Counts for the Ti Kα fluorescence peak (second column) are useful for relative abundance determinations within a scan. "Peak ratio" is the intensity ratio of the high and low energy pre-edge peaks (see text). Both formal valence and trivalent fraction are given along with one standard deviation values derived from multiple fittings of the pre-edge multiplet.

(Fig. 3c) is not accompanied by a change in valence. Measured V^{2+}/V^{tot} values range from 0.35 ± 0.05 to 0.72 ± 0.10 (1σ), averaging 0.58 ± 0.11 (Fig. 3d). Overall, in both crystals, the V valence is more homogeneous than the Ti valence.

3.1.2. V valence in Type B2 inclusions

In fassaite crystals in Type B1 inclusions, the Ti^{3+}/Ti^{tot} ratio tends to decrease from the cores to the rims of crystals (Simon et al., 1991), while fassaite in Type B2 inclusions is unzoned with respect to Ti^{3+}/Ti^{tot} (Simon and Grossman, 2006). This indicates that in B2s, unlike B1s, the residual liquid maintained equilibrium with the surrounding gas. Although this raises the possibility that B2s might be more reduced than B1s, the average Ti^{3+}/Ti^{tot} ratio calculated from a large suite of electron probe analyses of Type B2 fassaites is within error of the average for B1 fassaite (Simon and Grossman, 2006). For comparison with Type B1 inclusions, we measured V valence in fassaite in Allende Type B2 inclusion TS21, and the results are summarized in Fig. 4 and Table 3.

One traverse (Fig. 4a and b) is from the core to the rim of a monotonic, normally zoned single crystal, and the other (Fig. 4c and d) is across a sector-zoned grain that was discussed in some detail by Simon and Grossman (2006), shown here in Fig. 5. The latter traverse starts in a sector rich in the CaTs ($CaAlAlSiO_6$) pyroxene component and crosses into a diopside (Di)-rich sector. Both traverses show decreasing V contents with distance from the centers of the crystals (Fig. 4a and c). Like those for Ti (Simon and Grossman, 2006), the V valence trends are flat overall and erratic, with sudden fluctuations and no systematic trend with distance or sector. The average V valences of the two grains in TS21 are within 1σ of each other; the average V^{2+}/V^{tot} for Grain 4 is 0.48 ± 0.09 (Fig. 4b), and the average for Grain 5 is 0.60 ± 0.10 (Fig. 4d). The results of the measurements of V valence in the Type B2 inclusion are well within the range seen in Type B1 fassaite. In comparison, V in lunar volcanic glasses is predominantly V^{3+}, with an average valence of 2.90 ± 0.08 ($V^{2+}/V^{tot} = 0.10 \pm 0.08$; Sutton et al., 2005), and in terrestrial basalts V is predominantly V^{4+} (Sutton et al., 2005), as determined by the same technique as used here.

3.2. Pyroxene in rims on refractory inclusions

Many refractory inclusions are enclosed in sequences of mineralogically distinct layers, first described by Wark and

Table 3
Vanadium K XANES data for line scans of interior fassaite and a rim from Allende

Relative position (μm)	V abundance (counts)	Peak ratio	Valence	V^{2+}/V^{tot}	σ
Interior Fassaite					
Allende TS34 ZF2					
0	49,700	69	2.56	0.44	0.04
7	50,200	49	2.41	0.59	0.10
15	50,600	55	2.45	0.55	0.04
22	52,800	48	2.40	0.60	0.06
30	54,100	41	2.34	0.66	0.13
37	93,300	40	2.33	0.67	0.08
45	166,000	48	2.40	0.60	0.04
52	180,000	52	2.43	0.57	0.05
60	148,000	64	2.52	0.48	0.02
67	138,000	51	2.42	0.58	0.02
75	142,000	39	2.32	0.68	0.09
82	163,000	34	2.28	0.72	0.10
90	153,000	34	2.28	0.72	0.08
97	130,000	57	2.47	0.53	0.09
105	108,000	79	2.65	0.35	0.05
112	102,000	37	2.30	0.70	0.05
120	77,900	65	2.53	0.47	0.02
Allende TS34 PF6					
0	20,100	66	2.51	0.49	0.02
50	95,800	63	2.49	0.51	0.04
70	96,900	61	2.47	0.53	0.02
90	87,300	66	2.51	0.49	0.03
102	55,600	63	2.49	0.51	0.04
150	18,200	69	2.54	0.46	0.03
Allende TS21 Grain 4					
0	58,900	70	2.55	0.45	0.07
10	65,100	76	2.59	0.41	0.08
20	49,600	58	2.45	0.55	0.05
30	57,400	93	2.73	0.27	0.08
40	61,100	66	2.51	0.49	0.08
50	62,000	57	2.44	0.56	0.08
60	58,300	65	2.51	0.49	0.06
70	58,600	71	2.55	0.45	0.03
80	56,100	74	2.58	0.42	0.02
90	55,200	83	2.65	0.35	0.04
100	53,600	59	2.46	0.54	0.04
110	52,100	64	2.50	0.50	0.04
120	48,400	65	2.51	0.49	0.02
150	48,400	47	2.37	0.63	0.08
160	46,200	49	2.38	0.62	0.04
170	45,600	80	2.62	0.38	0.08
180	42,500	69	2.54	0.46	0.06
190	39,400	72	2.56	0.44	0.03
200	40,600	47	2.37	0.63	0.08
230	30,100	59	2.46	0.54	0.03
240	28,500	66	2.51	0.49	0.07
Allende TS21 Grain 5					
0	37,600	55	2.43	0.57	0.05
10	42,200	65	2.51	0.49	0.04
20	39,900	72	2.56	0.44	0.05
30	43,200	28	2.22	0.78	0.09
40	45,200	33	2.26	0.74	0.09
50	43,900	48	2.37	0.63	0.06
70	46,200	55	2.43	0.57	0.06
80	48,200	68	2.53	0.47	0.02
90	49,800	41	2.32	0.68	0.08

(*continued on next page*)

Table 3 (*continued*)

Relative position (μm)	V abundance (counts)	Peak ratio	Valence	V^{2+}/V^{tot}	σ
100	49,800	43	2.34	0.66	0.05
120	53,800	51	2.40	0.60	0.06
130	53,500	50	2.39	0.61	0.04
140	65,000	43	2.34	0.66	0.07
150	48,200	55	2.43	0.57	0.07
180	39,300	59	2.46	0.54	0.06
190	38,300	62	2.48	0.52	0.07
200	34,700	45	2.35	0.65	0.08
210	30,400	45	2.35	0.65	0.09
220	28,100	66	2.51	0.49	0.08
230	22,800	32	2.25	0.75	0.10
Rim					
Allende TS24 Rim 3					
0	19,500	47	2.36	0.64	0.10
2	19,400	50	2.39	0.61	0.08
4	24,200	42	2.33	0.67	0.09
6	22,400	44	2.35	0.65	0.11
8	17,100	43	2.33	0.67	0.04
10	14,000	57	2.44	0.56	0.07
12	9240	64	2.50	0.50	0.08

Counts for the V Kα fluorescence peak (second column) are useful for relative abundance determinations within a scan. "Peak ratio" is the intensity ratio of the high and low energy pre-edge peaks (see text). Both formal valence and divalent fraction are given along with one standard deviation values derived from multiple fittings of the pre-edge multiplet.

Lovering (1977), that must have formed after the host inclusions. A common sequence, from the CAI outward, consists of: a spinel ± perovskite layer; voids, melilite, or alteration products; and clinopyroxene. The pyroxene layer may be immediately adjacent to spinel and is commonly zoned from Ti-rich fassaite nearest the spinel layer to Ti-poor aluminous diopside over distances of ~10 μm (Wark and Lovering, 1977). The Ti-bearing pyroxene in the rims is therefore a potential recorder of nebular oxygen fugacity at some time after the formation of CAIs. ^{26}Mg–^{26}Al isotopic dating of rims indicates that they are $1–4 \times 10^5$ yr younger than their host inclusions (Taylor et al., 2004; J. Simon et al., 2005).

Also in the work of J. Simon et al. (2005), from electron probe data first reported by Dyl et al. (2005), the pyroxene in the rim of a compact Type A inclusion from Leoville, 144A, was found to have low CaO and high MgO contents relative to typical fassaite, such as that in the interior of the inclusion. The Ca contents were as low as 0.83 cations per formula unit, and those authors did not feel justified in normalizing the analyses to exactly one Ca cation per 6 oxygen anions. They also found that many of the analyses had ~4 cations per 6 oxygen anions with all Ti assumed to be Ti^{4+}, indicating negligible Ti^{3+} contents. Derivation of Ti^{3+}/Ti^{4+} ratios from electron probe analyses, however, is quite dependent upon how the data are normalized, and it is unclear how these analyses should be treated. To see if the pyroxene in Wark–Lovering rims truly is devoid of Ti^{3+}, we used XANES spectroscopy to determine the Ti valence in pyroxene in the rims of 144A and TS24, a large, fluffy Type A inclusion from Allende. The valence of V in the rim pyroxene of the latter inclusion was also measured (Table 3), and the results of the Ti measurements for both inclusions are given in Table 4.

Inclusion TS24 has a well-developed rim sequence, from the CAI outward to the matrix, of spinel and clinopyroxene, the latter zoned from Ti-, Al-rich fassaite to nearly pure diopside over ~20 μm. The spinel-pyroxene contacts are sharp. A view of a typical rim segment is shown in Fig. 6a. The pyroxene rim layer can be seen as a continuous gray band at the contact between the inclusion (CAI) and the meteorite matrix (mtx). Fig. 6b shows Area 2 Rim 3, one of the locations where EMP and XANES analyses were collected in traverses across the rim. The electron albedo of the pyroxene decreases with distance from the contact with spinel, reflecting decreasing Ti contents. The composition variation of the pyroxene across the rim is shown by the EMP data illustrated in Fig. 7. In addition to Ti oxide contents, those of Al_2O_3 also sharply decrease with increasing distance from the spinel contact, and there are complementary increases in MgO and in SiO_2 (not shown) over the inner ~7 μm, beyond which the compositions are uniform. The Ti, Mg and Si trends mimic typical core-to-rim zoning trends of fassaite in the interiors of Type B inclusions (Simon et al., 1991). Contents of V_2O_3 (<0.3 wt%) and Sc_2O_3 (below detection) are low, which is typical of low-Ti fassaite. The first five analyses of the Rim 3 traverse, those closest to the spinel contact, are presented in Table 5, with and without normalization to exactly one Ca cation as part of four total cations per 6 oxygen anions.

In addition to the features in common with interior fassaite, the rim pyroxene has some differences. These are illustrated in Fig. 8, which shows the inner half of the Area 2 Rim 3 traverse. Like many of the analyses of rim pyrox-

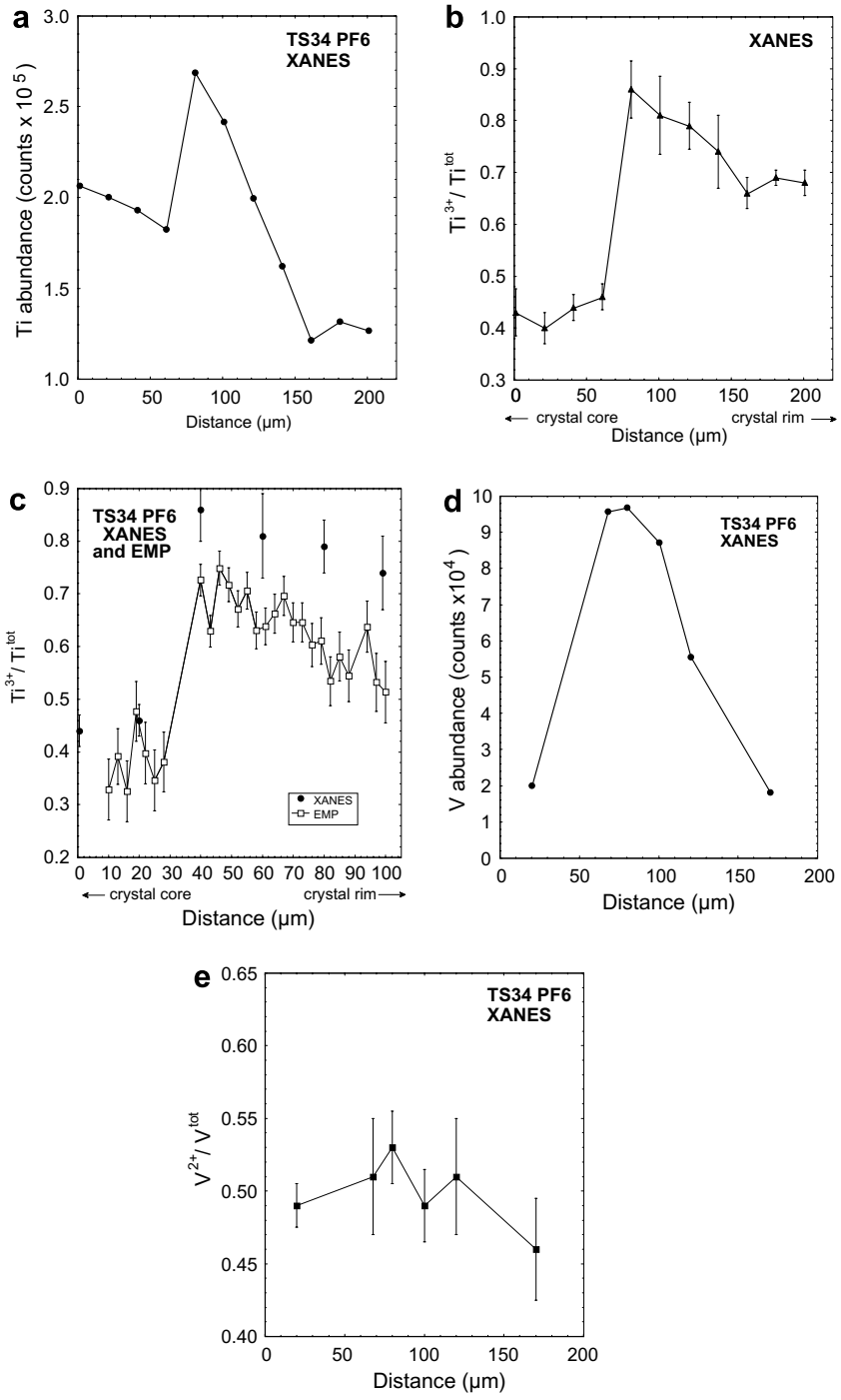

Fig. 2. Results of XANES traverses, from the crystal interior toward its rim, across the spike shown in Fig. 1. Uncertainties are 1σ. (a) Relative Ti abundance based on Ti K_α intensity, showing the sharp increase at the spike. (b) Ti^{3+}/Ti^{tot} ratio, also showing a sharp increase at the spike. (c) Comparison of XANES and EMP determinations of Ti valence across the spike. (d) Relative V abundance, from V K_α intensity. (e) V^{2+}/V^{tot}, showing no variation across the spike.

ene reported by J. Simon et al. (2005), the first two analyses of the traverse have ~4 total cations and <0.95 cations of Ca per 6 oxygen anions (Fig. 8a). Thus, no Ti^{3+} is indicated, whether or not the analyses are normalized to one Ca cation per 6 oxygen anions, as shown in Fig. 8b and Table 5. The other analyses in the traverse have >0.95 Ca per 6 oxygens, like "normal" fassaite, and the two with >4 wt% $TiO_2{}^{tot}$ have calculable Ti^{3+}, with Ti^{3+}/Ti^{tot} values of 0.55 ± 0.06 and 0.51 ± 0.07 with normalization to one Ca, and 0.66 ± 0.06 and 0.74 ± 0.08 without. The Ti^{3+}/Ti^{tot} values calculated for the pyroxene in the remainder of the traverse, with <4 wt% $TiO_2{}^{tot}$, are negative with normaliza-

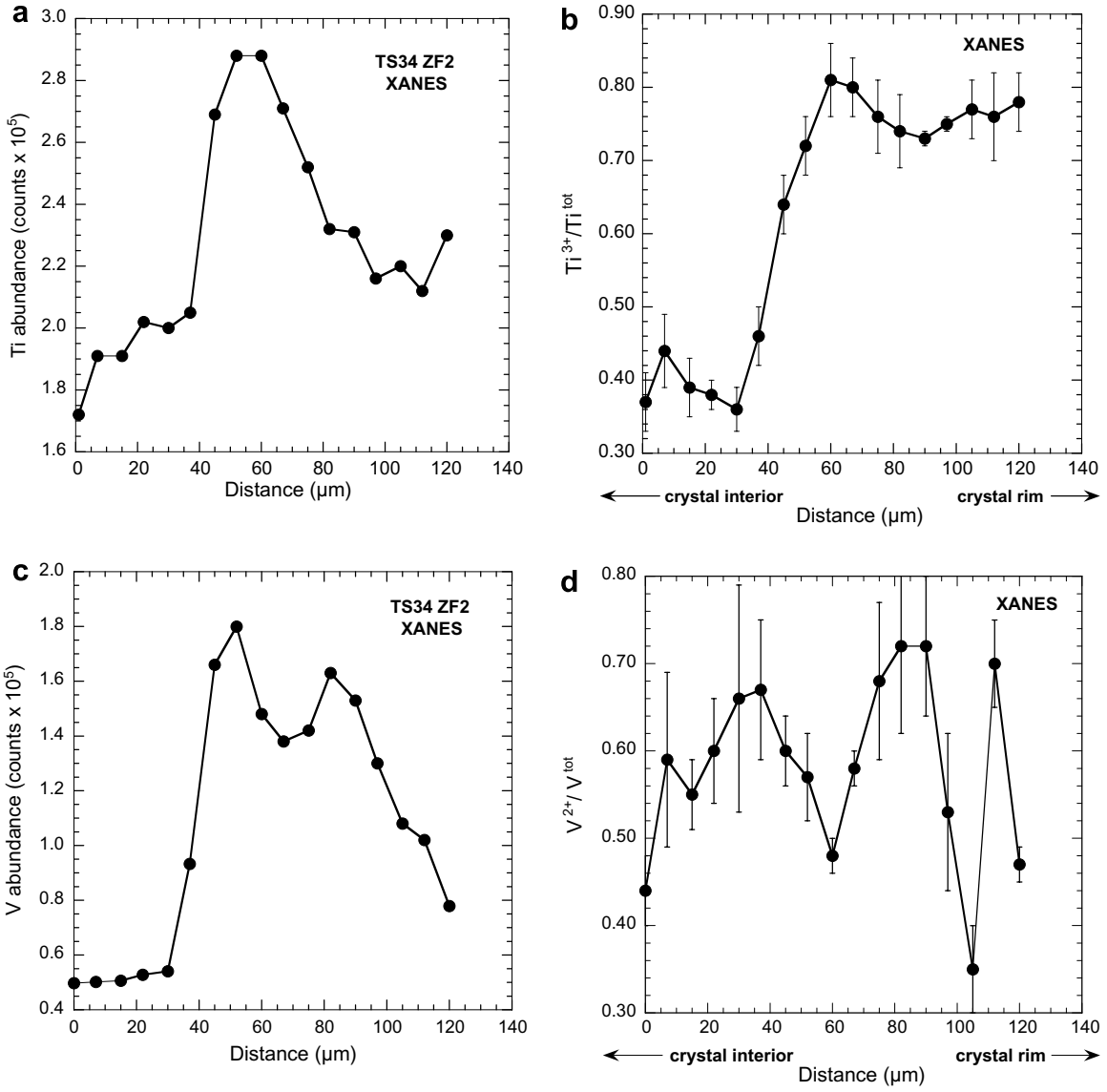

Fig. 3. Results of XANES traverses, from the crystal interior toward its rim, across a spike in another crystal, ZF2, in TS34. (a) Relative Ti abundance based on Ti K_α intensity, showing the sharp increase at the spike. (b) Ti^{3+}/Ti^{tot} ratio, also showing a sharp increase at the spike. (c) Relative V abundance, from V K_α intensity. (d) V^{2+}/V^{tot}, showing no systematic variation across the spike.

tion to one Ca, but the results of this calculation for pyroxene with such low Ti contents are not meaningful.

The XANES measurements of Ti valence along the same traverse show a quite different trend. In Fig. 9a, both Ti^{3+}/Ti^{tot} and relative Ti abundance in rim pyroxene are plotted as a function of distance from the contact with spinel. The Ti content drops sharply, as seen in the EMP data, but Ti^{3+}/Ti^{tot} does not. The ratio is nearly constant at ~0.53 through the first half of the traverse, then it decreases slightly to between 0.4 and 0.5. The average for the traverse is 0.48 ± 0.08. Unlike the EMP measurements of the first two spots in this traverse (Fig. 8b) and the analyses of the Leoville 144A rim by J. Simon et al. (2005), no Ti^{3+}-free pyroxene is observed. The measured Ti^{3+}/Ti^{tot} agrees with that calculated for the two EMP analyses that have >4 wt% $TiO_2{}^{tot}$ and positive Ti^{3+} after normalization to one Ca per 6 oxygens (analyses 3 and 4 in Table 5). A XANES traverse across the rim elsewhere in the thin section (TS24 Rim 1) also yielded fairly uniform Ti^{3+}/Ti^{tot} values, from 0.55 to 0.6, near the spinel contact, decreasing to ~0.45 at the outer edge. The average Ti^{3+}/Ti^{tot} for the traverse, 0.55 ± 0.07, is within error of that for Rim 3. The average Ti^{3+}/Ti^{tot} for all of our analyses of the pyroxene in the TS24 rim is 0.51 ± 0.08.

The valence of V was also determined for Area 2 Rim 3, and those results (relative abundances and V^{2+}/V^{tot}) are illustrated in Fig. 9b. Like the Ti traverse, abundance decreases with distance from spinel while the valence is constant, with an average V^{2+}/V^{tot} of 0.61 ± 0.06. Thus, the measurements of Ti and V valence in the rim yield fairly uniform ratios, with values that are well within the ranges seen in fassaite from inclusion interiors and

Please cite this article in press as: Simon S. B. et al, Valence of titanium and vanadium in pyroxene ..., *Geochim. Cosmochim. Acta* (2007), doi:10.1016/j.gca.2007.03.027

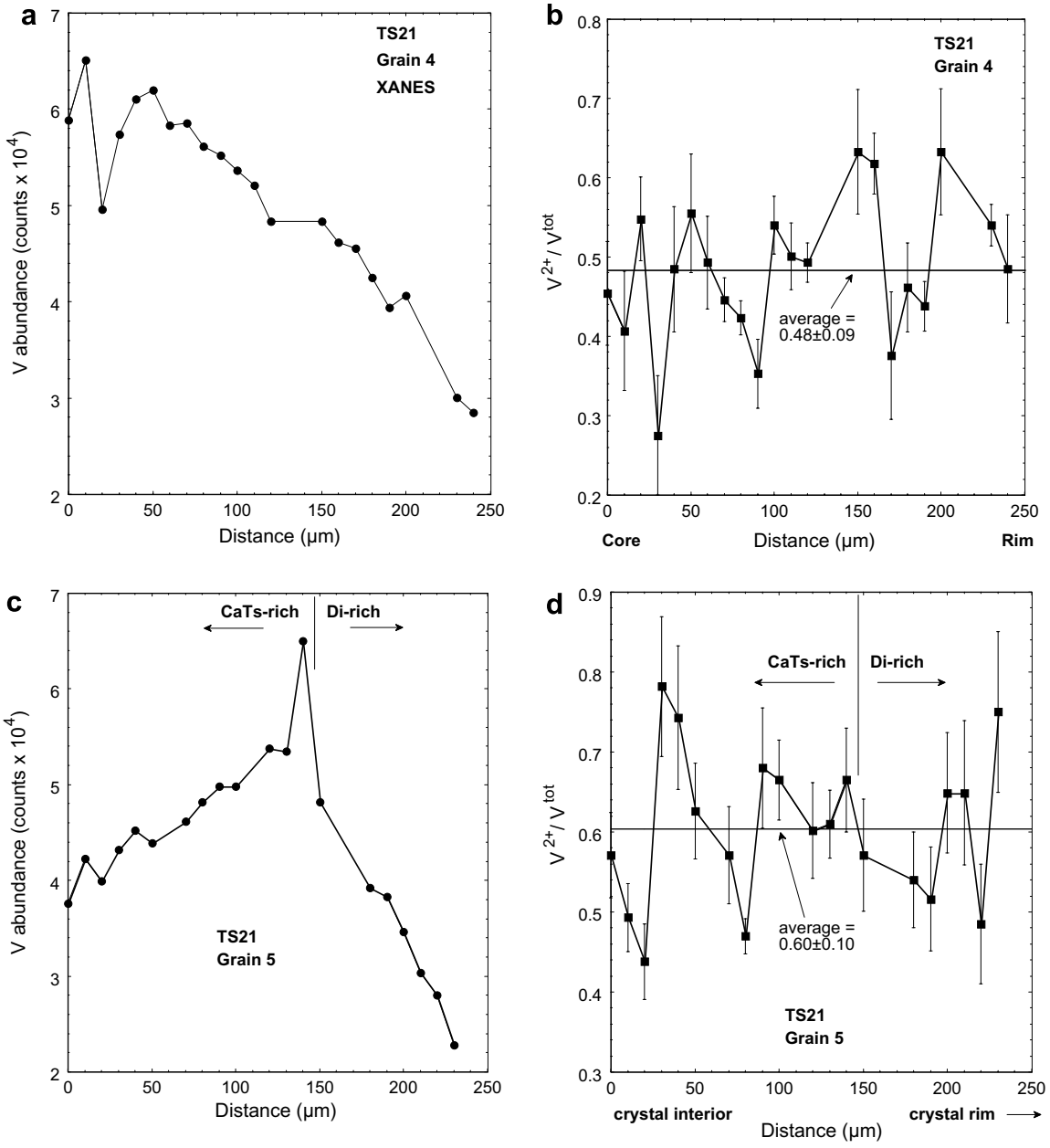

Fig. 4. XANES traverses across two fassaite grains in Allende Type B2 inclusion TS21. (a) Relative V abundance in Grain 4 vs. distance from the crystal core. (b) Vanadium valence in Grain 4. (c) Relative V abundances in a traverse across Grain 5, a sector-zoned crystal. The traverse started in the interior of the crystal in a CaTs-rich sector and crossed into a Di-rich sector, proceeding toward the edge of the crystal. (d) Vanadium valence in Grain 5.

are consistent with formation under highly reducing conditions.

Like the pyroxene layer in the rim sequence on TS24, the one in 144A is 10–20 μm thick. Its inner edge is, in various places, in contact with spinel ± hibonite, melilite, anorthite, or void space. Its outer edge is in contact with the meteorite matrix. Locally the layer contains inclusions of FeO-rich secondary alteration products and olivine (Fig. 10). As in TS24, electron probe analyses collected in traverses across the rim of 144A show decreasing Al_2O_3 and increasing MgO contents with increasing distance from the inner contact. Our analyses have 0–5.7 wt% TiO_2^{tot} (1.2 wt% average) and 0.5–6.8 wt% FeO (2.3 wt% average). Many have low Ca contents, <0.95 cation per 6 oxygen anions, compared to those of typical fassaite in the interiors of refractory inclusions, as was also found in this sample by J. Simon et al. (2005). A somewhat unusual feature of the present analyses is that FeO and CaO are anticorrelated (Fig. 11a) while no correlation is observed between MgO and FeO (Fig. 11b). Typically in ferromagnesian minerals, Fe substitutes for Mg and they are anticorrelated. Most of our analyses have TiO_2^{tot} contents that are too low for

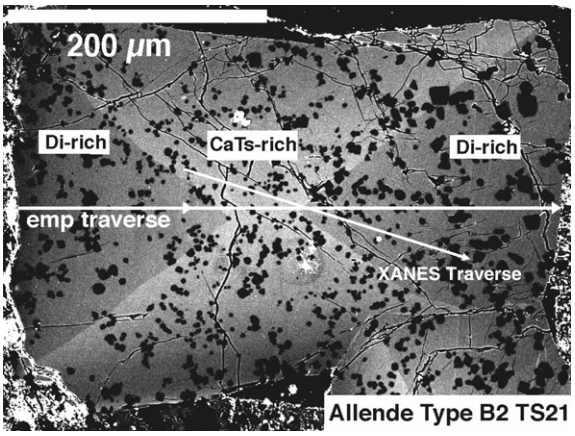

Fig. 5. Backscattered electron image of sector-zoned fassaite, Grain 5 in TS21. Also shown are paths along which electron probe (emp) and XANES data were collected. The emp results were reported by Simon and Grossman (2006).

accurate calculation of Ti^{3+}/Ti^{tot} ratios. Of our 96 analyses, only 10 have >4 wt% $TiO_2{}^{tot}$. Of these, five have calculated Ti^{3+}/Ti^{tot} ratios that are negative, and the other five have ratios ranging from 0.18 to 0.83, with an average of 0.42 ± 0.26, without normalization to one Ca cation per four total cations.

J. Simon et al. (2005) did not conduct traverses across the rim, but instead analyzed relatively Ti-rich pyroxene, with 2.3–7.7 wt% $TiO_2{}^{tot}$, found by X-ray mapping. Of their 26 analyses, 22 have >4 wt% $TiO_2{}^{tot}$, 15 with calculated Ti^{3+}/Ti^{tot} that are negative and 7 with positive Ti^{3+}/Ti^{tot}, ranging from 0.10 to 0.48 and averaging 0.31 ± 0.15, without normalization to one Ca cation per four total cations. The J. Simon et al. (2005) data also display a negative correlation, weaker than observed in our data, between CaO and FeO, and no correlation between MgO and FeO.

Results of the XANES measurements of Ti abundance and valence in the rim pyroxene of 144A (Table 4) are not as straightforward as those for TS24; analyses collected along six traverses in four different regions show significant proportions of Ti^{3+} while two traverses, in two other regions, include analysis points with Ti^{3+}/Ti^{tot} ratios that are nearly zero. In one of the latter cases, Area 5 (A5) Rim 2, the thickness of the rim approaches the depth of sampling for XANES analysis, ~10 μm, so unless the contacts are at high angles to the plane of the section, underlying material would have been sampled. As a test, we analyzed four matrix spots and obtained a mean Ti^{3+}/Ti^{tot} ratio of 0.08 ± 0.06 (1σ). This suggests that inclusion of underlying matrix material in the analysis volume can give results with erroneously low Ti^{3+}/Ti^{tot} ratios. The other area that yielded low Ti^{3+}/Ti^{tot} ratios (Dyl3 Rim) was also analyzed by J. Simon et al. (2005). We found that it contains inclusions of Ti-, Fe-bearing secondary alteration products (Fig. 10a). Inclusion of such oxidized materials in the analysis volumes probably lowered the Ti^{3+}/Ti^{tot} ratios in some of the XANES analyses of this area.

The results of a XANES traverse across a pure pyroxene rim layer (Area 5 Rim 3) are illustrated in Fig. 12. As in the rim on TS24, Ti contents decrease with increasing distance from the contact with the spinel layer. The profile of the Ti^{3+}/Ti^{tot} ratio is also quite like that of TS24; rather flat and between 0.5 and 0.6 near the spinel contact, decreasing to between 0.4 and 0.5 further away; the mean value is 0.49 ± 0.07 (1σ). Averages for four other XANES traverses of the rim of 144A are 0.38 ± 0.09, 0.50 ± 0.04, 0.44 ± 0.04, and 0.33 ± 0.02, and the average Ti^{3+}/Ti^{tot} for all 144A rim analyses excluding the A5 Rim 2 traverse is 0.41 ± 0.14. This indicates that there is significant Ti^{3+} in the rim pyroxene. The XANES analyses of rim pyroxene from two different inclusions yield average Ti^{3+}/Ti^{tot} ratios of 0.51 ± 0.08 and 0.41 ± 14; they are within error of each other at levels well within the range found for fassaite from the interiors of inclusions.

4. DISCUSSION

4.1. Fassaite in Type B refractory inclusion interiors

4.1.1. Formation conditions of Types B1 and B2 inclusions

Evidence for the formation of Types B1 and B2 inclusions at similar f_{O_2}s comes from Grossman et al. (in press), who derived the f_{O_2} for fassaite crystallization in CAI liquids by applying an experimental calibration of the Ti^{3+}/Ti^{4+} ratio in synthetic fassaite coexisting with melilite at a temperature of 1509 K. Their results are summarized in Fig. 13, a plot of $\log f_{O_2}$ *vs.* inverse temperature in Kelvins, for three vanadium buffers and the Ti_2O_3–TiO_2 (Ti^{3+}/Ti^{4+}) buffer, calculated from thermodynamic data for pure oxides (Chase, 1998). The Ti_2O_3–TiO_2 and VO-V_2O_3, or V^{2+}/V^{3+}, buffers are very close together, and have similar slopes. The variation of $\log f_{O_2}$ with inverse temperature during condensation of a system of solar composition is shown for reference. The point in Fig. 13 that represents the f_{O_2} of CAI formation is an average of 12 values obtained by Grossman et al. (in press); two reactions were applied to phase compositions in each of two compact Type A, two B1 and two B2 inclusions. These equilibria are not solely dependent upon the Ti^{3+}/Ti^{4+} ratios of the fassaite; they also include terms for the Diopside and Ca-Tschermak's pyroxene components and the coexisting melilite compositions. Their results yield an average $\log f_{O_2}$ of formation for Type B1 inclusions of -19.6 ± 0.7, within 1σ of the average of B2s, -19.1 ± 0.6, and within 1.5 log units of the f_{O_2} of a solar gas, $-18.1^{+0.2}_{-0.3}$, or IW-6.8, at the average calibration temperature, 1509 K. The experimental calibration of the CAI point plots well below the theoretical buffer curve for Ti_2O_3–TiO_2, reflecting the fact that the activities of these components in complex, real systems can differ markedly from those of the pure oxides.

The V^{2+}/V^{3+} ratios of fassaite in Types B1 and B2 coarse-grained refractory inclusions are virtually identical. Assuming they are primary and have not been significantly reset, and that the V^{2+}/V^{3+} equilibrium in this system is offset from the theoretical buffer curve in the same direction and by a similar amount as the Ti^{3+}/Ti^{4+} equilibrium is, the V^{2+}/V^{3+} ratios of fassaite are consistent with formation of Types B1 and B2 inclusions at similar f_{O_2}s, in a gas that was at least as reducing as one of solar composition. The

Table 4
Titanium K XANES data for rims from Allende and Leoville

Relative position (μm)	Ti abundance (counts)	Peak ratio	Valence	Ti^{3+}/Ti^{tot}	α
Allende TS24 Rim 1					
0.0	64,500	1.49	3.42	0.58	0.01
1.5	74,900	1.52	3.44	0.56	0.04
3.0	98,600	1.44	3.40	0.60	0.04
4.5	95,900	1.42	3.39	0.61	0.04
6.0	66,700	1.41	3.39	0.61	0.04
7.5	47,000	1.57	3.46	0.54	0.07
9.0	28,000	1.44	3.40	0.60	0.05
10.5	19,500	1.46	3.41	0.59	0.07
12.0	14,100	1.70	3.52	0.48	0.07
13.5	12,600	1.33	3.35	0.65	0.07
15.0	10,500	1.66	3.50	0.50	0.04
16.5	8820	1.80	3.57	0.43	0.04
18.0	8040	1.76	3.55	0.45	0.09
Allende TS24 Rim 3					
0.0	100,000	1.62	3.49	0.51	0.04
1.5	99,000	1.46	3.41	0.59	0.07
3.0	82,600	1.60	3.48	0.52	0.07
4.5	63,000	1.59	3.47	0.53	0.05
6.0	38,200	1.59	3.47	0.53	0.06
7.5	27,900	1.61	3.48	0.52	0.05
9.0	19,400	1.43	3.40	0.60	0.05
10.5	15,500	1.55	3.45	0.55	0.05
12.0	13,400	1.69	3.52	0.48	0.04
13.5	12,500	1.77	3.56	0.44	0.05
15.0	10,600	1.81	3.58	0.42	0.05
16.5	9420	1.98	3.66	0.34	0.08
18.0	8150	1.58	3.47	0.53	0.11
19.5	7270	1.93	3.64	0.36	0.06
21.0	6520	1.85	3.60	0.40	0.06
22.5	5630	1.90	3.62	0.38	0.06
Leoville 144A A5 Rim 3					
0	41,000	1.51	3.43	0.57	0.03
2	35,900	1.43	3.40	0.60	0.05
4	32,200	1.53	3.44	0.56	0.04
6	27,800	1.49	3.43	0.57	0.06
8	26,200	1.84	3.59	0.41	0.07
10	24,300	1.59	3.47	0.53	0.03
12	18,600	1.69	3.52	0.48	0.03
14	16,600	1.69	3.52	0.48	0.07
16	13,700	1.91	3.62	0.38	0.03
18	10,100	1.65	3.50	0.50	0.07
spot 1	11,400	1.73	3.54	0.46	0.07
spot 2	4200	1.67	3.51	0.49	0.05
spot 3	8300	1.21	3.29	0.71	0.11
Leoville 144A A5 Rim 2					
0	5890	2.15	3.74	0.26	0.02
3	6180	2.59	3.95	0.05	0.03
6	10,800	2.83	4.06	−0.06	0.02
9	16,100	2.37	3.84	0.16	0.03
Leoville 144A A6 Rim 1					
spot 1	5470	1.85	3.60	0.40	0.04
spot 2	4110	1.38	3.37	0.63	0.08
spot 3	30,700	2.31	3.81	0.19	0.03
spot 4	29,800	2.05	3.69	0.31	0.05

(*continued on next page*)

Table 4 (*continued*)

Relative position (μm)	Ti abundance (counts)	Peak ratio	Valence	Ti^{3+}/Ti^{tot}	α
Leoville 144A Dyl3 Rim					
0	14,800	2.03	3.68	0.32	0.03
6	9110	2.03	3.68	0.32	0.05
9	5860	2.69	3.99	0.01	0.11
12	4080	2.15	3.74	0.26	0.10
15	5250	2.37	3.84	0.16	0.04
18	5770	1.93	3.63	0.37	0.07
Leoville 144A A7B Rim 1					
0	264,000	1.81	3.58	0.42	0.04
2	136,000	1.65	3.50	0.50	0.05
4	54,000	1.50	3.43	0.57	0.13
Leoville 144A A7B Rim 2					
0	162,000	1.92	3.63	0.37	0.02
2	156,000	1.61	3.48	0.52	0.04
4	68,000	1.83	3.58	0.42	0.08
Leoville 144A A7B Rim 3					
0	43,300	2.11	3.72	0.28	0.16
2	41,200	2.04	3.68	0.32	0.06
4	21,600	2.05	3.69	0.31	0.06
5	32,100	2.08	3.71	0.29	0.09
6	22,200	1.98	3.66	0.34	0.19
8	17,500	1.80	3.57	0.43	0.15
Leoville 144A A7 Rim 1					
0	20,800	1.91	3.62	0.38	0.06
2	19,200	2.10	3.71	0.29	0.10
4	16,200	1.82	3.58	0.42	0.05
6	12,400	1.82	3.58	0.42	0.09

Positions given in numerical form reflect distances along line scans. Counts for the Ti Kα fluorescence peak (second column) are useful for relative abundance determinations within a scan. "Peak ratio" is the intensity ratio of the high and low energy pre-edge peaks (see text). Valence is listed both as formal valence and as trivalent fraction. Sigma is the one standard deviation of multiple fittings of the pre-edge multiplet.

fassaite–melilite equilibrium is the only experimentally calibrated f_{O_2} indicator that has ever been used to show that any assemblage in chondrites formed in a gas that was close to solar in composition.

4.1.2. Ti-, V-rich "spikes" in Type B1 inclusions

In some fassaite grains in Type B1 inclusions, sharp increases, or "spikes" in total Ti oxide content, total V oxide content, and in Ti^{3+}/Ti^{tot} are detected by both EMP and XANES in traverses across crystals. At the spikes, because Ti^{3+}/Ti^{tot} increases, a reduction event is indicated, and V would be expected to become more reduced at that point as well, increasing the V^{2+}/V^{tot} ratio. As Fig. 13 shows, a process that significantly increased the Ti^{3+}/Ti^{4+} ratio of a melt would be very likely to significantly increase its V^{2+}/V^{3+} ratio as well.

It is easy to understand why Ti^{3+} is more compatible in fassaite than Ti^{4+} (Simon et al., 1991). Substitution of Ti^{3+} for a divalent cation into the M1 crystallographic site in fassaite requires a coupled substitution of Al^{3+} for Si^{4+} in the tetrahedral site for charge balance, whereas substitution of Ti^{4+} into the M1 site requires substitution of two Al^{3+} cations for two Si^{4+} cations. In addition, the Ti^{3+} cation has a slightly larger radius than Ti^{4+}, giving it a better fit into the M1 site (Papike et al., 2005).

In contrast, it is not clear which valence state of vanadium should be preferred by pyroxene. We infer from the titanium systematics that the spikes reflect reduction events in which the interiors of Type B1 inclusions equilibrated with the nebular gas after having been isolated from it by melilite mantles (Simon and Grossman, 2006). From the locations of the relevant buffer curves (Fig. 13), an increase in Ti^{3+}/Ti^{4+} would be accompanied by an increase in V^{2+}/V^{3+}. The increase in V content at the spike would therefore indicate that V^{2+} is more compatible than V^{3+}, but based on its similarity to Ti^{3+} in terms of ionic radius, the V^{3+} cation would be a better fit in the M1 site than would V^{2+} and on that basis should be more compatible in pyroxene. On the other hand, V^{2+} could enter pyroxene without a charge-balancing coupled substitution in the tetrahedral site, which could make it more compatible than V^{3+}. A series of experiments that are in progress should lead to a determination of pyroxene/liquid distribution coefficients as a function of oxygen fugacity and vanadium oxidation state, down to V^{2+}.

Although it is likely that valence state changes originally accompanied the V abundance changes at the spikes, none are detected, and this is not yet understood. One possible explanation is that there were originally sharp increases in V^{2+}/V^{3+} at the spikes but they were erased in an *in situ*

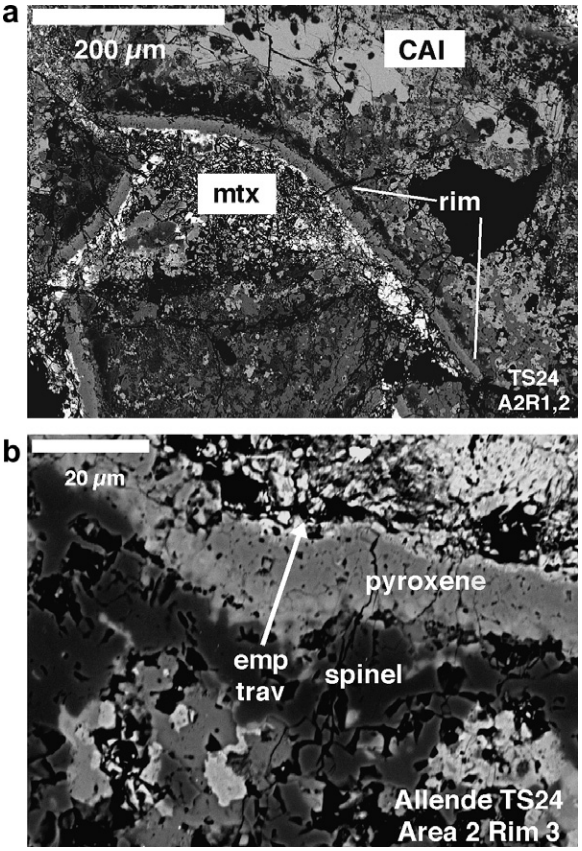

Fig. 6. Backscattered electron images of the rim of TS24. (a) General view of a rim segment, showing the relationship between the host inclusion (CAI), the rim, and the Allende matrix (mtx). Note the spinel layer (black) of the rim and the pyroxene layer adjacent to it, zoned from relatively Ti-rich (light) to Ti-poor (dark). (b) Location of EMP and XANES traverses (arrow), Area 2, Rim 3.

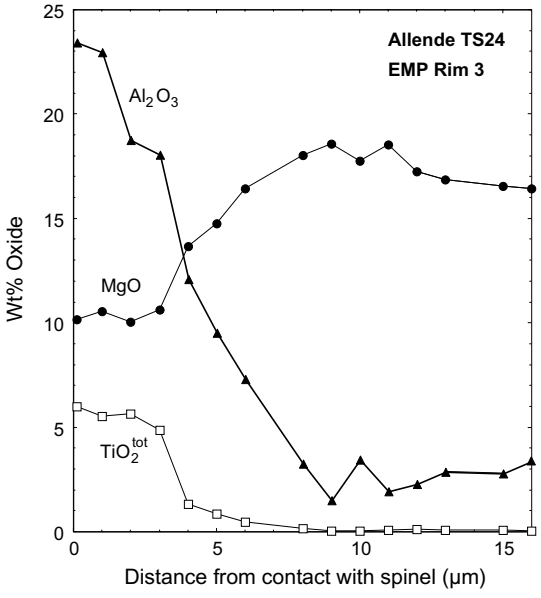

Fig. 7. Oxide abundances (wt%) measured by electron microprobe (EMP) in the TS24 Area 2 Rim 3 traverse.

homogenization reaction involving later transfer of electrons with Ti, according to the reaction

$$Ti^{4+} + V^{2+} \iff Ti^{3+} + V^{3+}$$

There is so much more Ti than V present that only a small proportion of the Ti^{4+} would be required to change its valence to convert "excess" V^{2+} to V^{3+}. Note, however, that not only is there no spike in V^{2+}, but the V valence is uniform across the traverse. We do not know if the electron transfer process should be expected to completely homogenize the valence of vanadium, as is observed in the present case. Charge transfer on cooling of silicate melt has been observed between Fe^{3+} and Cr^{2+}, oxidizing the latter to the trivalent state and reducing the former to Fe^{2+} (Berry et al., 2006). Once fassaite/liquid distribution coefficients for V^{2+} and V^{3+} are determined, the crystal chemical behavior of V in pyroxene, and the lack of a V valence state change at the spikes will be better constrained.

4.2. Pyroxene in rims on refractory inclusions

The Ti-bearing pyroxene in the rims on some CAIs is an important recorder of f_{O_2} during its formation, which, according to the work of J. Simon et al. (2005), occurred $1–3 \times 10^5$ yr after the formation of CAIs. Taylor et al. (2004) also dated a Wark–Lovering rim and found it to be 4.4×10^5 yr younger than its host CAI. J. Simon et al. (2005) concluded that rims formed at f_{O_2}s at least ~6 log units higher than the f_{O_2} of CAI formation, and that inclusions experienced a dramatic change in oxygen fugacity that occurred over a relatively short time, probably as a result of transport from a reducing environment to a relatively dust-enriched, oxidizing one. Their f_{O_2} estimate was based on their conclusion that the pyroxene in the rim has negligible Ti^{3+}, from the average Ti^{3+} content for all of their electron probe analyses of -0.03 ± 0.02 cations per 6 oxygen anions. Recall, however, that of the 26 analyses listed in the appendix of J. Simon et al. (2005), four have <4 wt% TiO_2^{tot} and are unlikely to give accurate Ti^{3+}/Ti^{tot} values. Of the remaining 22 analyses, 15 have ⩾4 cations per 6 oxygens and calculated Ti^{3+} contents that are zero or negative, and the other seven have <4 cations per 6 oxygens and Ti^{3+} contents that are positive. The average Ti^{3+}/Ti^{tot} for these seven analyses is 0.31 ± 0.15. Among our data for Leoville 144A, only ten analyses have >4 wt% TiO_2^{tot}. Of these, five have calculated Ti^{3+} contents that are negative. The other five have positive Ti^{3+} and an average Ti^{3+}/Ti^{tot} of 0.42 ± 0.26. The averages of the positive Ti^{3+}/Ti^{tot} values obtained from electron probe analyses of rim pyroxene with >4 wt% TiO_2^{tot} for both our data and those of J. Simon et al. (2005) are within 1σ of the average of the XANES analyses, 0.41 ± 0.14. If the electron probe analyses with positive Ti^{3+} are of spots containing pure pyroxene and the analyses with negative Ti^{3+} are contaminated by an adjacent phase, then there may be no discrepancy between the XANES and electron probe determinations of Ti valence in pyroxene. We suggest that this is the case.

Fig. 14 is a plot of Ca and Al vs. total cations per 6 oxygen anions for analyses with oxide totals >95 wt%, >4 wt% TiO_2^{tot} and from 3.95–4.05 total cations, with data from

Table 5
The first five analyses of the traverse of Rim area 3 plotted in Figs. 7 and 8

Sample	1	2	3	4	5
MgO (wt%)	10.15	10.54	10.07	10.65	13.68
Al_2O_3	23.43	22.96	18.76	18.06	12.13
SiO_2	35.44	37.15	40.65	41.86	47.45
CaO	23.06	23.38	25.19	25.03	25.02
Sc_2O_3	0.03	0.03	0.02	0.05	0.01
Ti as TiO_2	6.01	5.52	5.63	4.87	1.31
V_2O_3	0.17	0.28	0.25	0.24	0.10
Cr_2O_3	0.06	0.06	0.10	0.06	0.04
FeO	0.49	0.41	0.13	0.15	0.39
Ti_2O_3	−0.34	0.23	3.31	3.21	1.08
TiO_2	6.22	5.10	1.93	1.26	0.10
Sum	98.72	100.14	100.41	100.56	99.98
Cations per 6 oxygen anions					
Si	1.312	1.354	1.486	1.524	1.720
^{IV}Al	0.688	0.646	0.514	0.476	0.280
^{VI}Al	0.335	0.341	0.295	0.299	0.238
Mg	0.560	0.573	0.549	0.578	0.739
Fe	0.015	0.012	0.004	0.004	0.012
Sc	0.001	0.001	0.001	0.002	0.000
V	0.005	0.008	0.007	0.006	0.003
Cr	0.002	0.002	0.003	0.002	0.001
Ti^{3+}	−0.011	0.007	0.101	0.098	0.033
Ti^{4+}	0.178	0.144	0.053	0.035	0.003
Ca	0.915	0.913	0.987	0.976	0.972
Ti^{3+}/Ti^{tot}	−0.064	0.048	0.656	0.739	0.925
After normalization to one calcium cation and 6 oxygen anions					
Ti_2O_3 (wt%)	−3.79	−3.35	2.77	2.18	−0.14
TiO_2	9.88	8.93	2.50	2.37	1.45
Sum	98.92	100.39	100.44	100.65	100.13
Cations					
Si	1.276	1.316	1.480	1.512	1.704
^{IV}Al	0.724	0.684	0.520	0.488	0.296
^{VI}Al	0.270	0.275	0.285	0.280	0.217
Mg	0.545	0.557	0.546	0.573	0.732
Fe	0.015	0.012	0.004	0.004	0.012
Sc	0.001	0.001	0.001	0.002	0.000
V	0.005	0.007	0.007	0.006	0.003
Cr	0.002	0.002	0.003	0.002	0.001
Ti^{3+}	−0.120	−0.105	0.085	0.067	−0.004
Ti^{4+}	0.283	0.252	0.069	0.065	0.040
Ca	1.000	1.000	1.000	1.000	1.000
Ti^{3+}/Ti^{tot}	−0.740	−0.714	0.551	0.505	−0.125

J. Simon et al. (2005) and from our work plotted separately. Among the analyses with negative Ti^{3+}, there is a positive correlation between Al content and total cations and a negative one between Ca and total cations. In contrast, these trends are not observed among the analyses with positive Ti^{3+}, and contents of these elements should not covary with each other or with total cations due to crystal-chemical substitutions. These trends are, however, consistent with contamination of analyses (that may actually have Ti^{3+}) with input from an adjacent Ca-poor, Al-rich phase with >4 cations per 6 oxygens, such as spinel. Because spinel has a higher cation:oxygen ratio than pyroxene, addition of spinel to a pyroxene analysis increases the cation total and noticeably decreases the amount of Ti^{3+} calculated. Also plotted on Fig. 14 are arrows showing trends of spinel addition for the pyroxene analysis that has 0.93 Al, 0.94 Ca and 4 total cations per 6 oxygen anions. The calculated trends for spinel addition provide reasonably good fits to the anal-

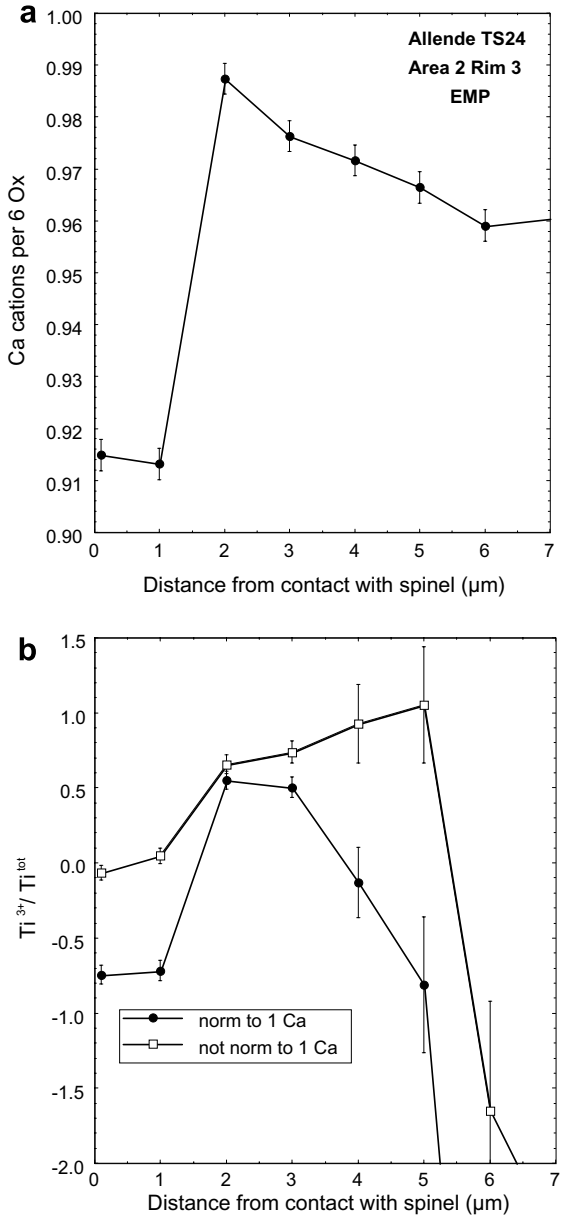

Fig. 8. (a) Abundances of Ca cations per 6 oxygen anions in the inner part of the Area 2 Rim 3 pyroxene traverse. The two points nearest the spinel layer have much lower Ca contents than the next five. (b) Ti^{3+}/Ti^{tot} ratios calculated for the analyses, both with (solid circles) and without (open squares) normalization to one Ca per 6 oxygen anions. Uncertainties are 1σ, based on counting statistics.

yses with >4 cations per 6 oxygens even though only a single starting composition was used. The ends of the arrows correspond to 10% spinel addition. Thus, small contributions, ~1–7%, from adjacent spinel could account for the negative Ti^{3+}/Ti^{tot} ratios and low Ca contents observed in some of the analyses of the relatively Ti-rich pyroxene in the rim of 144A. The innermost two analyses of the electron microprobe traverse of the TS24 rim (Fig. 8, Table 5), with low Ca and no Ti^{3+}, probably also reflect contamination by spinel.

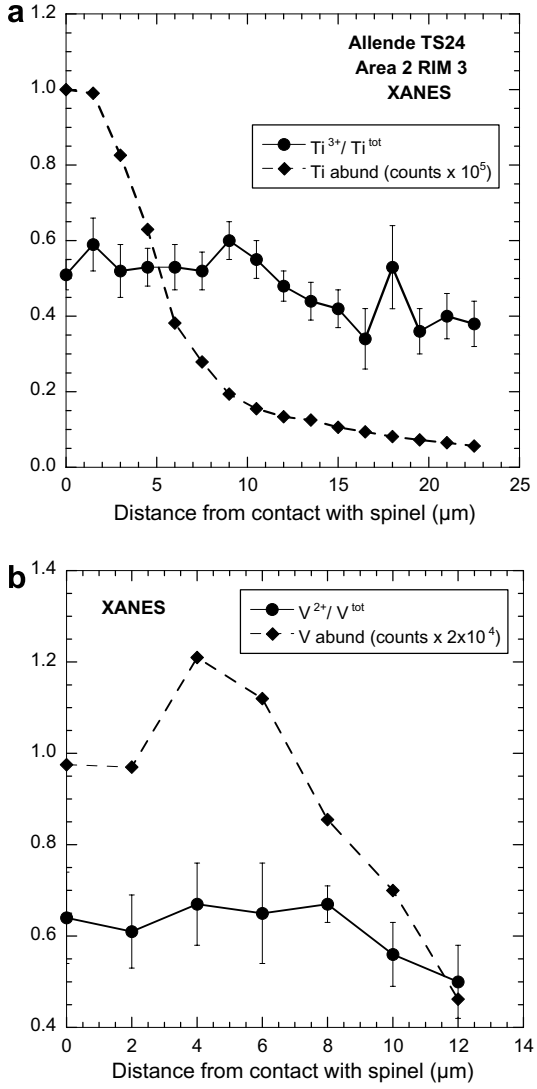

Fig. 9. Results of XANES traverses across pyroxene in Area 2 Rim 3 in TS24. Relative Ti and V abundances are based on K_α intensities. (a) Titanium content and valence. (b) Vanadium content and valence. The valence measurements show significant proportions of Ti^{3+} and V^{2+}.

On the other hand, the negative correlation between FeO and CaO observed in our suite of analyses of the rim of 144A, especially in those with <4 wt% $TiO_2{}^{tot}$ and >4 cations per 6 oxygen anions, suggests mixing of pyroxene with an FeO-rich, CaO-poor component, probably olivine, either in the matrix or included in the rim. Many of our points were collected along traverses that extended across the rim, from the CAI toward and very close to the matrix, and could have small contributions from adjacent phases. The XANES data may reflect this also in the decrease in Ti^{3+}/Ti^{tot} in the rim of TS24 from ~0.55–0.60 to ~0.40–0.45. Admixture of an olivine component as an analytical artifact can also explain how the analyses can contain FeO and have undisturbed Mg–Al isotopic systematics; the Fe is not actually substituting for Mg in the pyroxene.

Please cite this article in press as: Simon S. B. et al, Valence of titanium and vanadium in pyroxene ..., *Geochim. Cosmochim. Acta* (2007), doi:10.1016/j.gca.2007.03.027

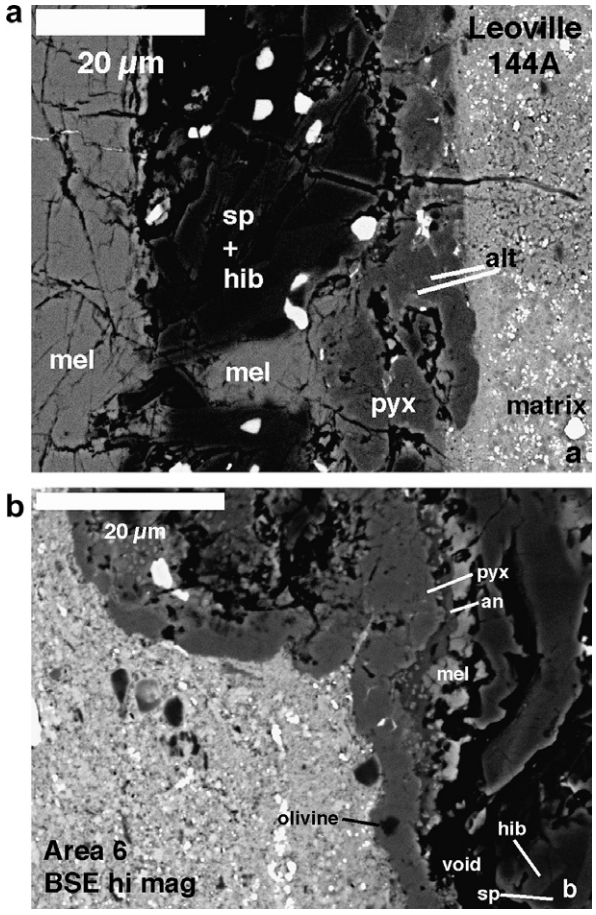

Fig. 10. Backscattered electron images of the rim of Leoville 144A. (a) Area containing visible Fe-rich secondary alteration products (alt). (b) Area with an inclusion of olivine. an, anorthite; hib, hibonite; mel, melilite; pyx, pyroxene.

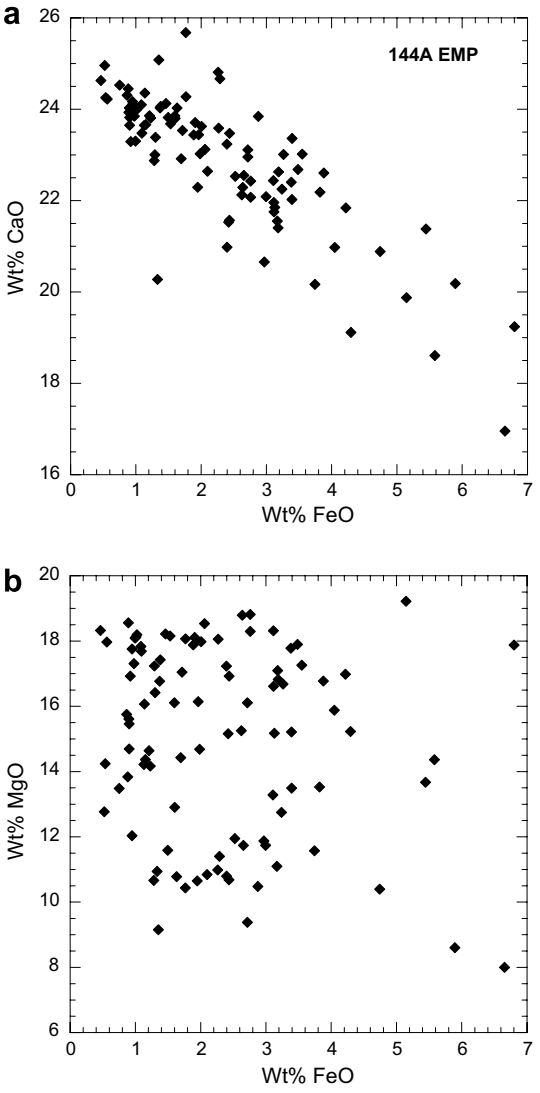

Fig. 11. Electron probe analyses of pyroxene in the rim of Leoville 144A collected for this study. (a) CaO vs. FeO. (b) MgO vs. FeO. CaO contents are anticorrelated with those of FeO, but MgO contents are not.

Both the average Ti and V valences determined for rim pyroxenes by XANES, and average Ti^{3+}/Ti^{tot} ratios determined by electron probe for pure pyroxene analyses are within the ranges of values seen in interior fassaites, and the presence of both Ti^{3+} and V^{2+} in rim pyroxene is strong evidence for the formation of rims on CAIs at an oxygen fugacity very close to that expected for a solar gas. The rim of Leoville 144A underwent secondary alteration at some unknown point, and oxidized iron entered the rim to widely varying degrees, forming rare, FeO-bearing phases that are heterogeneously distributed.

5. CONCLUSIONS

We investigated valence variations across Ti-, V-rich concentration "spikes" in fassaite in Type B1 inclusions, V valence in fassaite in Type B2 inclusions, and both Ti and V valence in fassaite in rims on refractory inclusions using electron probe analysis (Ti) and XANES spectroscopy (Ti and V). We found:

(1) Although V contents and Ti^{3+}/Ti^{tot} increase sharply at the spikes, V^{2+}/V^{tot} does not. There may have been a reduction event followed by equilibration of V in an electron transfer reaction with Ti; the origin of the spikes is still not well understood.
(2) V contents decrease from core to rim while V valence is uniform across fassaite grains in the interiors of Type B2 inclusions. Thus, in both B1 and B2 inclusions, the V valence trend is uniform as a function of distance across a fassaite grain.
(3) The V^{2+}/V^{tot} values observed in fassaite in Type B2 inclusions, 0.4–0.7, are within the range seen for fassaite from Type B1 inclusions. They reflect equilibration under highly reducing conditions and are consistent with formation in a solar gas.

Please cite this article in press as: Simon S. B. et al, Valence of titanium and vanadium in pyroxene ..., *Geochim. Cosmochim. Acta* (2007), doi:10.1016/j.gca.2007.03.027

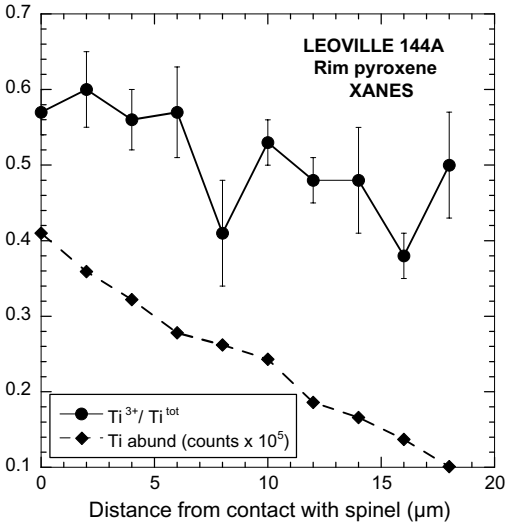

Fig. 12. Results of a XANES traverse across pyroxene in the rim of Leoville 144A. As in the TS24 rim, Ti contents decrease sharply and Ti^{3+}/Ti^{tot} ratios decrease slightly with increasing distance from the spinel rim layer.

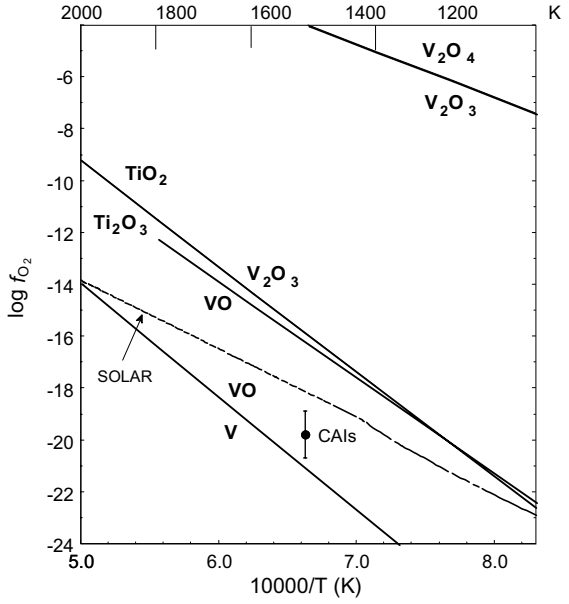

Fig. 13. Theoretical buffer curves for V–VO, VO–V_2O_3, V_2O_3–V_2O_4 (solid, no symbols) and Ti_2O_3–TiO_2 (dashed) equilibria, calculated from thermodynamic data for pure oxides. The curve for a condensing system of solar composition (Allende Prieto et al., 2002) is shown for reference. The data point represents the f_{O_2} of fassaite crystallization in CAIs, as determined from equilibria involving coexisting melilite and fassaite of known composition in Allende inclusions for the average experimental equilibration temperature of 1509 K, by Grossman et al. (in press).

(4) The pyroxene in Wark–Lovering rims on coarse-grained refractory inclusions has Ti^{3+}/Ti^{tot} and V^{2+}/V^{tot} like those observed for fassaite in the interiors of inclusions, suggesting that inclusions and their rims both formed under low-f_{O_2} conditions similar to those of a solar gas.

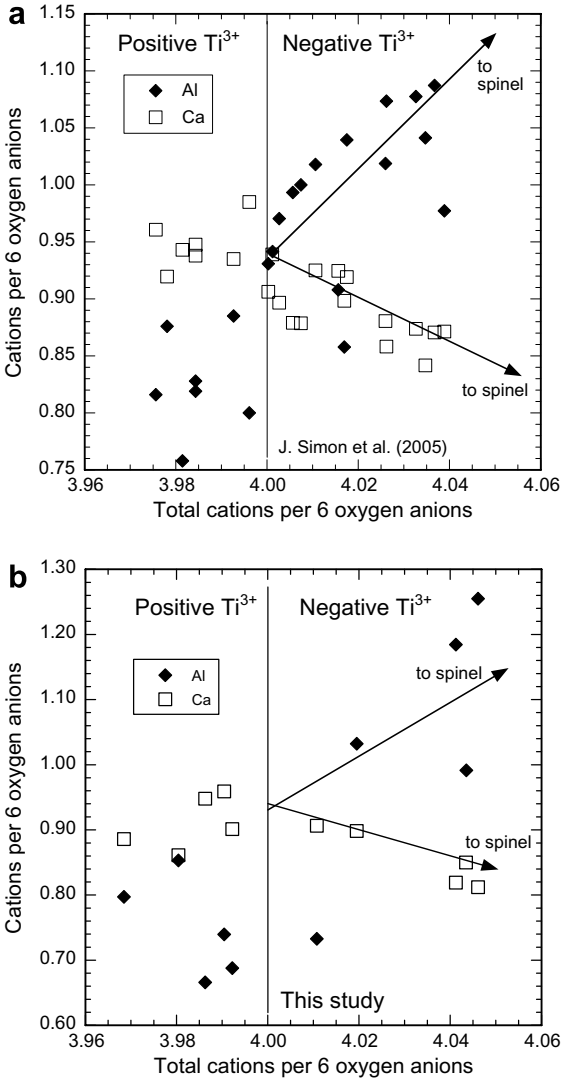

Fig. 14. Abundances of Al and Ca cations per 6 oxygen anions in (a) data from J. Simon et al. (2005) and (b) this work for analyses with >4 wt% TiO_2^{tot}. Analyses with negative calculated Ti^{3+} components show a positive correlation between Al and total cations and a negative correlation between Ca and total cations, along trends consistent with spinel addition (arrows).

ACKNOWLEDGMENTS

We thank E. Young and K. Dyl for twice lending us sample 144A for analysis and for sharing their data. G. Rossman (Caltech) and K. Evans (Australian National University) kindly provided standards. This paper was reviewed by H. Connolly and M. Petaev. This work was supported by NASA through Grant NNG05GG00G (LG). XANES measurements were performed at GeoSoilEnviroCARS (GSECARS), Sector 13, Advanced Photon Source (APS), Argonne National Laboratory. GSECARS is supported by NSF-Earth Sciences (EAR-0622171), and DOE-Geosciences (DE-FG02-94ER14466). Use of the Advanced Photon Source was supported by the U.S. Department of Energy, Office of Science, Office of Basic Energy Sciences, under Contract No. DE-AC-02-06CH11357, and funding is gratefully acknowledged.

REFERENCES

Allende Prieto C., Lambert D. L., and Asplund M. (2002) A reappraisal of the solar photospheric C/O ratio. *Astrophy. J. Lett.* **573**, L137–L140.

Beckett J. R. (1986) The origin of calcium-, aluminum-rich inclusions from carbonaceous chondrites: an experimental study. Ph.D. Thesis, University of Chicago.

Berry A. J., O'Neill H. St. C., Scott D. R., Foran G. J., and Shelley J. M. G. (2006) The effect of composition on Cr^{2+}/Cr^{3+} in silicate melts. *Am. Mineral.* **91**, 1901–1908.

Chase, Jr., M. W. (1998) NIST-JANAF Thermochemical Tables, fourth edition. *J. Phys. Chem. Ref. Data, Monogr.*(9), 1963.

Dowty E., and Clark J. R. (1973) Crystal structure refinement and optical properties of a Ti^{3+} fassaite from the Allende meteorite. *Am. Mineral.* **58**, 230–242.

Dyl K. A., Simon J. I., Russell S. S., and Young E. D. (2005) Rapidly changing oxygen fugacity in the early solar nebula recorded by CAI rims. *Lunar Planet. Sci. XXXVI*. Lunar Planet. Inst., Houston. #1531 (abstr.).

Eng P. J., Rivers M. L., Yang B. X., and Schildkamp W. (1995) Microfocusing 4-keV to 65-keV X-rays with bent Kirkpatrick–Baez mirrors. *Proc. SPIE Int. Soc. Opt. Eng.* **2516**, 41–51.

Eng P. J., Newville M., Rivers M. L., and Sutton S. R. (1998) Dynamically figured Kirkpatrick–Baez micro-focusing optics. In *X-Ray Microfocusing: Applications and Technique* (ed. I. McNulty). Proc. SPIE 3449, pp. 145–156.

Grossman L. (1972) Condensation in the primitive solar nebula. *Geochim. Cosmochim. Acta* **36**, 597–619.

Grossman L. (1975) Petrography and mineral chemistry of Ca-rich inclusions in the Allende meteorite. *Geochim. Cosmochim. Acta* **39**, 438–451.

Grossman L. (1980) Refractory inclusions in the Allende meteorite. *Ann. Revs. Earth Planet. Sci.* **8**, 559–608.

Grossman L., Beckett J. R., Fedkin A. V., Simon S. B., and Ciesla F. J. (in press) Redox conditions in the solar nebula: Observational, experimental, and theoretical constraints. *Rev. Mineral., Oxygen in the Solar System*.

Kirkpatrick P., and Baez A. V. (1948) Formation of optical images by X-rays. *J. Opt. Soc. Am.* **38**, 766–774.

Krause M. O., and Oliver J. H. (1979) Natural widths of atomic K and L levels, K_α X-ray lines and several KLL Auger lines. *J. Phys. Chem. Ref. Data* **8**, 329–338.

MacPherson G. J., and Grossman L. (1979) Melted and non-melted coarse-grained Ca-, Al-rich inclusions in Allende. *Meteoritics* **14**, 479–480 (abstr.).

Papike J. J., Karner J. M., and Shearer C. K. (2005) Comparative planetary mineralogy: Valence state partitioning of Cr, Fe, Ti and V among crystallographic sites in olivine, pyroxene, and spinel from planetary basalts. *Am. Mineral.* **90**, 277–290.

Pouchou J. L., and Pichoir F. (1984) A new model for quantitative X-ray microanalysis. Part I: application to the analysis of homogeneous samples. *Rech. Aerosp.* **1984-3**, 13–38.

Prewitt C. T., Shannon R. D., and White W. B. (1972) Synthesis of a pyroxene containing trivalent titanium. *Contrib. Mineral. Petr.* **35**, 77–82.

Schreiber H. D., and Balazs G. B. (1982) Vanadium as an oxygen geobarometer in basaltic magmas: the further development of a geochemical electromotive force series in silicate melts. *Lunar Planet Sci. XIII*. Lunar Planet. Inst., Houston, 692–693 (abstr.).

Simon J. I., Young E. D., Russell S. S., Tonui E. K., Dyl K. A., and Manning C. E. (2005) A short timescale for changing oxygen fugacity in the solar nebula revealed by high-resolution ^{26}Al–^{26}Mg dating of CAI rims. *Earth Planet. Sci. Lett.* **238**, 272–283.

Simon S. B., and Grossman L. (1991) Profiles of Ti^{3+}/Ti^{tot} ratios in zoned fassaite in Allende refractory inclusions. *Meteoritics* **26**, 395 (abstr.).

Simon S. B., and Grossman L. (2006) A comparative study of melilite and fassaite in Types B1 and B2 refractory inclusions. *Geochim. Cosmochim. Acta* **70**, 780–798.

Simon S. B., Grossman L., and Davis A. M. (1991) Fassaite composition trends during crystallization of Allende Type B refractory inclusions. *Geochim. Cosmochim. Acta* **55**, 2635–2655.

Simon S. B., Davis A. M., and Grossman L. (1992) Evidence for changes in redox state during crystallization of Allende Type B1 inclusions. *Meteoritics* **27**, 289–290 (abstr.).

Simon S. B., Sutton S. R., and Grossman L. (2005) Valence of Ti and V in fassaite: A recorder of oxygen fugacity during crystallization of coarse-grained refractory inclusions. *Workshop on Oxygen in the Earliest Solar System*. LPI Contrib. No. 1278, 35 (abstr.).

Simon S. B., Sutton S. R., and Grossman L. (2006) Measurement of Ti^{3+}/Ti^{4+} ratios in pyroxene in Wark–Lovering rims: Evidence for formation in a reducing solar nebula. *Lunar Planet Sci. XXXVII*. Lunar Planet. Inst., Houston. #1772 (abstr.).

Smith J. V., and Rivers M. L. (1995) Synchrotron X-ray microanalysis. In *Microprobe Techniques in the Earth Sciences* (eds. P. J. Potts, J. F. W. Bowles, S. J. B. Reed and M. R. Cave). Chapman and Hall, London, UK, pp. 163–233.

Stolper E., and Paque J. M. (1986) Crystallization sequences of Ca–Al-rich inclusions from Allende: The effects of cooling rate and maximum temperature. *Geochim. Cosmochim. Acta* **50**, 1785–1806.

Sutton S. R., and Rivers M. L. (1999) Hard X-ray synchrotron microprobe techniques and applications. In *Synchrotron X-ray Methods in Clay Science, CMS Workshop Lectures*, vol. 9 (eds. D. G. Schulze, J. W. Stucki and P. M. Bertsch). The Clay Minerals Society, Boulder, CO, pp. 146–163.

Sutton S. R., Simon S., Grossman L., Delaney J. S., Beckett J., Newville M., Eng P., and Rivers M. (2002a) Evidence for divalent vanadium in Allende CAI fassaite and implications for formation conditions. *Lunar Planet Sci. XXXIII*. Lunar Planet. Inst., Houston. #1907 (abstr.).

Sutton S. R., Bertsch P. M., Newville M., Rivers M., Lanzirotti A., and Eng P. (2002b) Microfluorescence and microtomography analyses of heterogeneous earth and environmental materials. In *Applications of Synchrotron Radiation in Low-Temperature and Environmental Science*, *Reviews in Mineralogy & Geochemistry*, **49** (eds. P. Fenter, M. Rivers, N. Sturchio and S. Sutton). Mineralogical Society of America, Washington, D.C., pp. 429–483.

Sutton S. R., Karner J. M., Papike J. J., Delaney J. S., Shearer C. K., Newville M., Eng P., Rivers M., and Dyar M. D. (2005) Vanadium K edge XANES of synthetic and natural basaltic glasses and application to microscale oxygen barometry. *Geochim. Cosmochim. Acta* **69**, 2333–2348.

Taylor D. J., McKeegan K. D., and Krot A. N. (2004) ^{26}Al in Efremovka CAI E44L-Resolved time interval between interior and rim formation in a highly fractionated compact Type A CAI. *Workshop Chondrites Protoplanetary Disk*. SOEST, University of Hawaii Pub. No. 04-03, pp. 197–198 (abstr.).

Wark D. A., and Lovering J. F. (1977) Marker events in the early evolution of the solar system: Evidence from rims on Ca–Al-

Please cite this article in press as: Simon S. B. et al, Valence of titanium and vanadium in pyroxene ..., *Geochim. Cosmochim. Acta* (2007), doi:10.1016/j.gca.2007.03.027

rich inclusions in carbonaceous chondrites. *Proc. Lunar Sci. Conf* **8**, 95–112.

Waychunas G. A. (1987) Synchrotron radiation XANES spectroscopy of Ti in minerals: Effects of Ti bonding distances, Ti valence and site geometry on absorption edge structure. *Am. Mineral.* **72**, 89–101.

Yang B. X., Rivers M. L., Schildkamp W., and Eng P. (1995) GeoCARS micro-focusing Kirkpatrick–Baez mirror bender development. *Rev. Sci. Instrum.* **66**, 2278–2280.

Associate editor: Alexander N. Krot